Title
Group 2 innate lymphoid cells promote inhibitory synapse development and social behavior

Author
Barron, Jerika J.

Publication Date
2022

Group 2 innate lymphoid cells promote inhibitory synapse development and social behavior

by
Jerika Barron

DISSERTATION
Submitted in partial satisfaction of the requirements for degree of
DOCTOR OF PHILOSOPHY

in

Biomedical Sciences

in the

GRADUATE DIVISION
of the
UNIVERSITY OF CALIFORNIA, SAN FRANCISCO

Approved:

DocuSigned by:
Xianhua Piao
85E65FF36F664D9...

Xianhua Piao
Chair

DocuSigned by:
Anna Victoria Molofsky
D...

Anna Victoria Molofsky

DocuSigned by:
Ari Molofsky
D...

Ari Molofsky

DocuSigned by:
Samuel Pleasure
05586C7D64D24A2...

Samuel Pleasure

Committee Members

Dedication

In loving memory of my grandmother, Mary Bass

Acknowledgements

The experience of earning a PhD involves immense learning and growth, which I am lucky to have achieved in part due to the generous and intelligent people I have shared my time with. I will always be inspired by the many people that have contributed to my journey. I want to foremost thank my mentor, Anna Molofsky, for her guidance and mentorship during my graduate training. I am a vastly better scientist, writer, and critical thinker thanks to her training. I am grateful for the support and encouragement she showed me through the highs and lows of the last six years, both in and out of research. She taught me to be more confident in myself, rigorous in my work, and to embrace the challenge of the unknown - qualities I know I will use far into my future.

I also want to thank Ari Molofsky, who I was lucky to work closely with since the inception of my thesis project. His guidance and enthusiasm were integral to my training in immunology and tackling this project. I am grateful to the other members of my thesis committee, Xian Piao and Sam Pleasure, for their insight and encouragement over the years that helped push my project forward through the turns it took. There are many others at UCSF that I can't list in full - my rotation labs, exam committees, the BMS program, my graduate cohort of 2016, and ImmunoX - to which I am grateful to have had enlightening conversations and the opportunity to work with.

This project could not have succeeded without the invaluable work of my co-authors and colleagues and the stimulating environment they created. Collaboration was key to this project and to my growth as a scientist. Thank you to "Team Meninges" – especially Madelene Dahlgren, Jorge Ortiz-Capena, and Nick Mroz - for courageously melding neuroscience and immunology. To my other co-authors – Sunrae Taloma, Ilia Vainchtein, Leah Dorman, and Caroline Escoubas – for lending your skillful expertise and excitement. A special thank you to each and every member of the Molofsky lab that I have had the pleasure to work with from the onset – Hiromi Nakao-Inoue, Phi Nguyen, Marci Rosenberg, Nick Silva, Rafael Han, Haruna Nakajo, Christian Lagares-Linares, Carol Kim, Richard Jin, Ricky Guajardo, and Dongkyu Kim. I have learned invaluable

skills and lessons from all of these people, along with gaining such enthusiastic and supportive friends.

I must also credit my early research experiences with helping me reach this point. Thanks to my first mentor, Kerry Thompson at Occidental College, who introduced me to neuroscience and gave me the chance to try my hand at research. Thanks to Rusty Gage and Baptiste Jaeger at the Salk for giving me the opportunity to push myself as a young scientist and sparking my love of neuroimmunology.

I have been fortunate to have a special trio of women in my life who have cheered for me and supported me in my endeavors, academic and otherwise. My mom, Marlene Barron, thank you for your eternal optimism and confidence in me. My aunt, Debi Pohto, thank you for always believing in me and lifting me to reach higher. My beloved late grandmother, Mary Bass, thank you for your overflowing pride and teaching me to cherish the privilege of pursuing education. I wouldn't be where I am as a first-generation college student, and now doctorate, without their support and sacrifices. I am also deeply appreciative to the rest of my family who have encouraged me and supported me in this pursuit, especially my uncle Dave Pohto and my in-laws, Dee and Jeff Margolis and family.

Finally, I am immensely grateful to my husband, Mitch Margolis, for his support for more than a decade. Thank you for your love, encouragement, and steadying presence from the start and every day since – this success is yours too.

Contributions

This manuscript contains data adapted from the following research manuscript submitted for publication:

Barron, J.J., Taloma, S.E., Dahlgren, M.W., Mroz, N.M., Ortiz-Carpena, J., Dorman, L.C., Vainchtein, I.D., Escoubas, C.C., Molofsky, A.B.*, Molofsky, A.V.*. "**Group 2 innate lymphoid cells promote inhibitory synapse development and social behavior",** (2022).

Conceptualization, J.J.B., A.V.M, and A.B.M.; Methodology, J.J.B., A.V.M, and A.B.M. Investigation, J.J.B., S.E.T., M.W.D. J.O.C., N.M.M., L.C.D., I.D.V. and C.C.E.; Writing – Original Draft, J.J.B., A.B.M. and A.V.M.; Writing – Review & Editing, all co-authors; Funding Acquisition, A.V.M, and A.B.M.; Resources, A.V.M, and A.B.M.; Supervision, A.V.M, and A.B.M.

We thank the A.V. and A.B. Molofsky labs, R.M. Locksley, and J.L. Rubenstein for helpful comments on the manuscript. We thank R.M. Locksley for generous sharing of mouse strains; M. Khierbeck and V. Sohal for guidance and resources in behavioral analyses; and K. Bender for electrophysiology guidance. We thank the UCSF Laboratory for Cell Analysis Core, the UCSF Parnassus Flow Core (RRID:SCR_018206 and DRC Center Grant NIH P30 DK063720), UCSF Biological Imaging and Development Core, and UCSF Laboratory Animal Resource Center for instruments and services.

J.J.B. was supported by a NIMH Ruth L. Kirchstein Predoctoral National Research Service Award (F31MH122207). M.W.D. was supported by the Swedish Research Council (2018-00307). A.V.M. was supported by a Pew Scholars Award, the Brain and Behavior Research Foundation, NIMH (R01MH125000 and R01MH119349), and NINDS (1R01NS126765). A.B.M. is supported by the NINDS (1R01NS126765), NHLBI (1R01HL142701), NIAID (401AI162806) and the UCSF Department of Laboratory Medicine.

Abstract

Group 2 innate lymphoid cells promote inhibitory synapse development and social behavior

Jerika J. Barron

In early brain development, the formation and remodeling of neuronal synaptic connections is critical to forming functional neural circuits. The innate immune system plays essential roles in neurodevelopment, including in synapse remodeling, but the immune cells and signals that contribute are not well defined. Innate lymphocytes are the most recently discovered member of the innate immune arsenal, whose developmental expansion and activation make them potential mediators of brain-immune communication during synapse formation. Here we show that a subset of innate lymphocytes (group 2 innate lymphoid cells, ILC2s) populates the developing brain meninges and is required for cortical inhibitory synapse maturation and adult social behavior. ILC2s produced a surge of their canonical cytokine Interleukin 13 (IL-13) between postnatal days 5-15. Loss of ILC2s decreased cortical inhibitory synapse numbers in the postnatal period and led to impaired social recognition memory in adulthood. Postnatal administration of IL-13 or ILC2s into the brain ventricles was sufficient to drive an increase in inhibitory synapses. Deletion of the IL-4/IL-13 receptor (*Il4ra*) specifically from inhibitory neurons, but not myeloid cells, also reduced inhibitory synapses and impaired adult social behavior. These data define novel type 2 immune signaling that mediates lymphocyte-neuron communication in early life and shapes adult brain function.

Table of Contents

List of Figures

Chapter 1: Introduction

The innate immune system monitors and promotes healthy organ development, including in the brain. Concurrently, immune dysfunction has both epidemiologic and genetic links to neurodevelopmental and psychiatric disorders (Bohlen et al., 2019; Bennett and Molofsky, 2019; Knuesel et al., 2014). These disorders profoundly impact social behavior and cognition and are linked to changes in excitatory/inhibitory synaptic balance (Rubenstein, 2010; Rubenstein and Merzenich, 2003) that can lead to long-lasting alterations in neural synaptic connectivity (Marín, 2016). Importantly, lymphocytes and their cytokines can directly impact adult cognition, memory, and social behaviors (Alves De Lima et al., 2020 a; Alves de Lima et al., 2020 b; Brombacher et al., 2017; Derecki et al., 2010; Filiano et al., 2016; Herz et al., 2021; Kipnis, 2016; Ribeiro et al., 2019). However, the cellular crosstalk and the developmental timing of these effects are only beginning to be explored. Defining the developmental impact of central nervous system (CNS)-associated lymphocytes is critical to a mechanistic understanding of the brain-immune interface.

Homeostatic immune responses occur locally within well-regulated tissue niches. Innate immune cells such as macrophages, innate lymphoid cells (ILCs), and innate-like unconventional T cells (*e.g.* $\gamma\delta$ T cells) are deposited during embryogenesis and early postnatal life, where they locally mature their effector functions concomitant with organ maturation (Gasteiger et al., 2015). These tissue-resident innate immune responses are particularly critical during early life, where they can act prior to the full maturation and expansion of adaptive B and T cells. ILCs are the most recently discovered and enigmatic member of the innate immune arsenal (Kotas and Locksley, 2018). Their subtypes closely mirror the types of T cells that expand later in life (*i.e.* type 1, type 2, type 3/17). Unlike many T cells, ILCs produce cytokines within hours and in response to local tissue cues, rather than over days and in response to specific antigens. Group 2 innate lymphoid cells (ILC2s) represent one of these subsets and are dominant producers of the type 2 cytokine

Interleukin 13 (IL-13). ILC2-driven remodeling is critical to limiting helminths and driving allergic pathology, but also impacts tissue development (Kobayashi et al., 2019; Saluzzo et al., 2017). In the CNS, ILC2s are protective in a spinal cord injury model and in aging (Fung et al., 2020; Gadani et al., 2016), but their role in brain development is unknown.

Here we show that ILC2s promote early-life neuronal inhibitory synapse development and adult social behavior. We found that ILC2s expand perinatally within the mouse brain meninges and produce a burst of their canonical cytokine IL-13 between postnatal days 5-15, a key timepoint for neuronal synapse maturation and refinement. Loss of ILC2s led to a reduction in cortical inhibitory synapses in early postnatal life and impaired social recognition memory, while other behavioral measures, such as object recognition and contextual memory, remained intact. This inhibitory synaptic defect was phenocopied by global deletion of the IL-13/ IL-4 receptor subunit *Il4ra*, whereas intracranial injection of ILC2s or IL-13 was sufficient to increase inhibitory synapse numbers. We identified inhibitory neurons as a direct and relevant target of IL-13 via conditional deletion experiments that phenocopied the inhibitory synapse defect and impacted adult social behaviors. These data support a model in which IL-13 derived from activated, early life ILC2s signals directly to GABAergic neurons to promote inhibitory synapse maturation. More broadly, they suggest that innate immune signaling can dynamically shape neuronal connectivity during key periods of brain development.

Chapter 2: Innate lymphocytes expand in the developing brain meninges

The CNS immune environment includes tissue-resident cells both within the brain parenchyma, primarily comprised of microglia, and in the brain boundaries, including meningeal- and perivascular-associated immune cells. Unlike in the parenchyma, meningeal boundary regions contain a full complement of immune cell types, including macrophages, dendritic cells, and innate and adaptive lymphocytes that mirror tissue immune niches in other organs (Alves De Lima et al., 2020; Rua and McGavern, 2018). Recent studies have characterized the meningeal cellular composition in embryogenesis and adulthood (DeSisto et al., 2020; Mrdjen et al., 2018; Van Hove et al., 2019; Zelco et al., 2021), but not during postnatal development when most synaptogenesis takes place. To study this period, we first performed single cell RNA sequencing (scRNAseq) of immune and non-immune skull-associated meningeal cells on postnatal day (P)14 (**Fig. 2.1A).** To complement our previous studies showing a role for the alarmin Interleukin 33 (IL-33) in postnatal synaptic development (Vainchtein et al., 2018; Han et al., 2021) and given that IL-33 can induce ILC2 activation, we also compared mice deficient in IL-33 (*Il33*$^{mcherry/mcherry}$) to controls (*Il33*$^{mcherry/+}$). To better capture rare populations, we selectively enriched to increase representation of lymphocytes (CD45^{+}CD11b^{-}, non-myeloid immune cells) and stromal cells (gp38^{+}CD31^{-}; **Fig. 2.2A**). Unsupervised clustering revealed a multitude of immune and stromal populations (**Fig. 2.1B**; 12,544 cells; quality control in **Fig. 2.2B-D**), consistent with published datasets. As expected, IL-33 expression was enriched in subpopulations of meningeal fibroblasts (**Fig. 2.2E**) suggesting they may be a relevant meningeal source that is discrete from well-described glial and neuronal IL-33 sources in the brain parenchyma.

Given that both ILCs and T cells are abundant cytokine producers, we further analyzed these populations by sub-clustering all non-B lymphocytes (Cluster 9). This revealed a predominance

of innate lymphocytes in early life, including ILC2s (*Cd3e*$^{-}$*, Gata3*$^{+}$) and innate-like gamma-delta ($\gamma\delta$) T cells (*Cd3e*$^{+}$*, Rorc*$^{+}$), as well as smaller populations of putative NK cells (*Cd3e*$^{-}$*, Tbx21*$^{+}$*, Eomes*$^{+}$) and group 1 innate lymphoid cells (ILC1s; *Cd3e*$^{-}$*, Tbx21*$^{+}$*, Eomes*$^{-}$; **Fig. 2.1C-E**). In contrast, adaptive immune cells such as CD4^{+} T cells (*Cd3e*$^{+}$*, Cd4*$^{+}$) were relatively rare in this early developmental period. Furthermore, all innate lymphocyte subsets expressed canonical transcription factors and effector genes required for cytokine production, whereas early-life T cells did not. This was true for ILC2s (*Gata3, Il5, Il13),* $\gamma\delta$ *T* cells *(Rorc, Il17),* and NK cells *(Tbx21, Eomes, Ifng)* (**Fig. 2.1D-E**). There was a modest impact of IL-33 on the meningeal immune profile, where ILC2s from IL-33 deficient mice (*Il33*$^{mcherry/mcherry}$) were normal in number (flow cytometry, not shown) but had a reduction in activation markers and cytokine transcripts *(Il13, Areg, Cxcl2)* relative to controls (*Il33*$^{+/mcherry}$; **Fig. 2.2F-G**). This suggested that IL-33 is just one of multiple signals regulating early-life meningeal ILC2 activation, as described in other tissues (Van Dyken et al., 2016).

We also observed a relative abundance of innate lymphocytes by flow immunophenotyping over the course of development (P0-P100; **Fig. 2.1F, Fig. 2.2H**). Intracellular protein staining revealed that innate and innate-like lymphocytes produced transcription factors required for cytokine production including GATA3, Tbet, EOMES, and RORγt (**Fig. 2.1G,** gating in **Fig. 2.2H**). Thus, innate immune cells are a predominant lymphocyte population in the developing brain meninges that are poised for cytokine production.

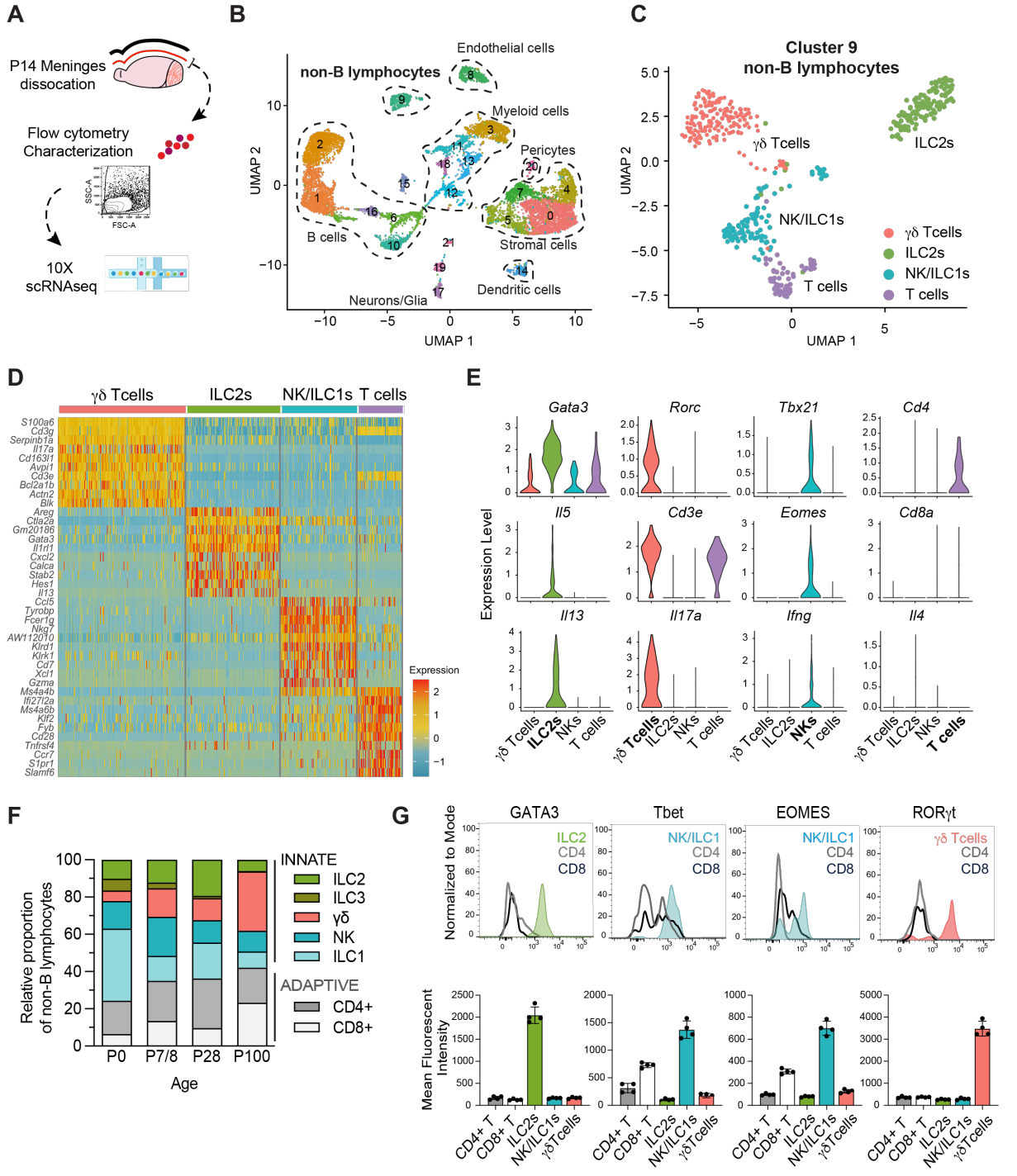

Figure 2.1: Innate lymphocytes expand in the developing brain meninges.

A) Schematic of postnatal day (P)14 dural meninges isolation for flow cytometry and single cell mRNA sequencing.

B) Unsupervised clustering (UMAP) of 12,544 cells from pooled P14 meninges (enriched for stromal cells and non-myeloid immune cells) with cell-type assignments based on marker gene expression. See Fig.

Fig. 2.2A-D for flow cytometry gating, quality control metrics, and cell-type assignment. See Supplemental Table 2.1 for list of cluster-defining genes.

C) Sub-clustering of non-B lymphocytes from panel B, including T cells and innate lymphoid cells (Cluster 9; 477 cells). See Supplemental Table 2.2 for list of cluster-defining genes.

D) Heatmap of top cluster-defining genes by log fold change for non-B lymphocytes in panel C used for cell-type assignments.

E) Expression of lineage-defining and effector genes in non-B lymphocytes from panel C.

F) Quantification by flow cytometry of innate and adaptive lymphocytes in meninges across development (pre-gated on viable $CD45^{+}CD11b^{-}CD19^{-}$ cells, shown as a relative proportion among the indicated cell types; Number of mice per age: P0 n=2; P7/8 n=4; P28 n=3; P100 n=4). Gating strategy in Fig. 2.2H.

G) Representative flow histograms (top) and quantification (bottom) of protein expression of lineage-defining transcription factors including GATA3 (type 2), Tbet (type 1), EOMES (type 1), and RORγt (type 3/17). Age P28. Dots represent mice. Gating strategy in Fig. 2.2H.

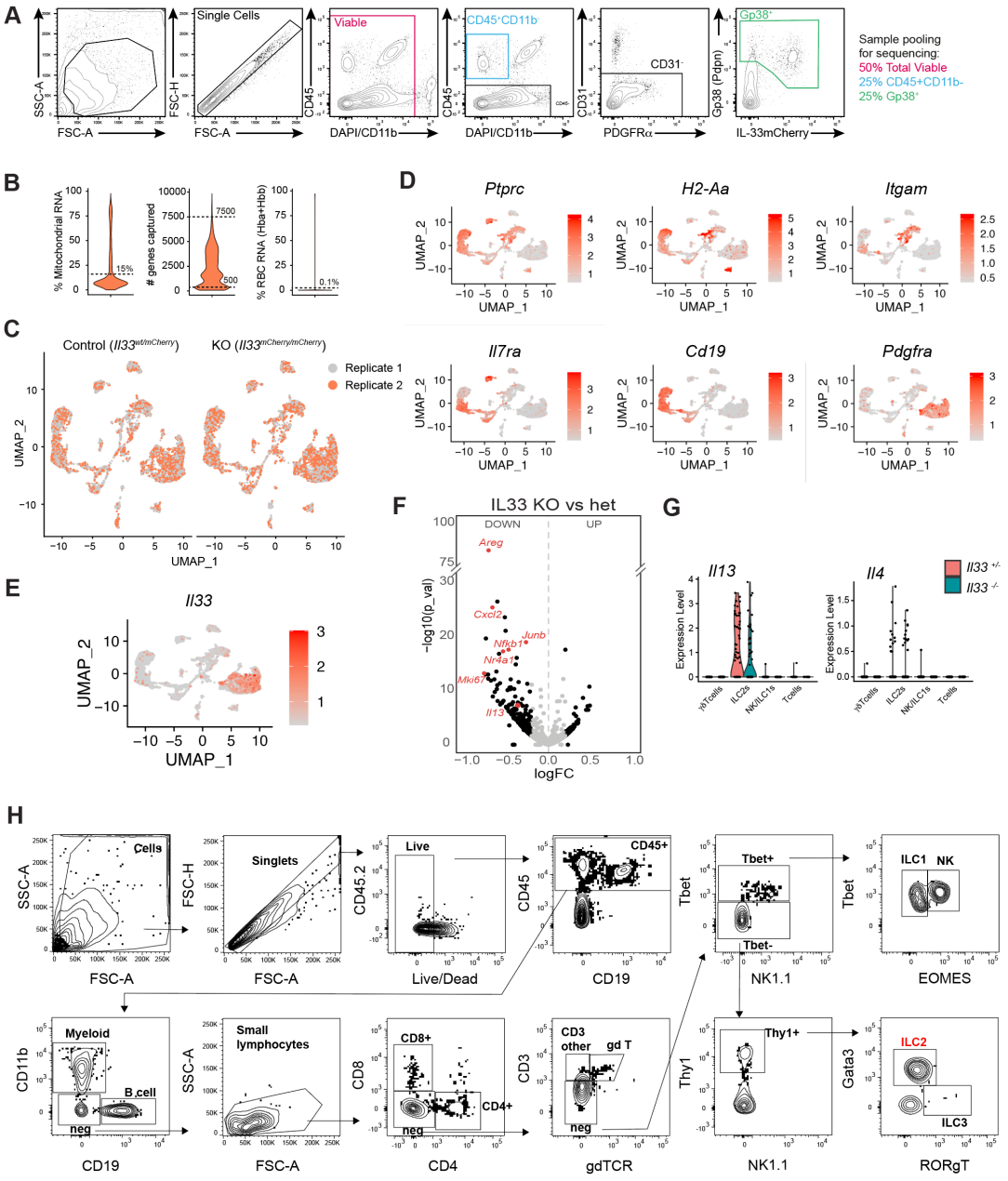

Figure 2.2: Gating and quality control for meningeal immune profiling.

A) Gating strategy for fluorescence activated cell sorting of P14 dural meninges for scRNAseq in Fig. 2.1B, showing gates used to enrich non-myeloid immune cells (blue, $CD45^{+}CD11b^{-}$, 25% of final pool) and stromal cells (green, $gp38^{+}CD31^{-}$, 25% of final pool) and total viable (red, 50% of final pool).

B) Quality control metrics for single cell sequencing, thresholds indicated with dotted lines.

C) Overlay of samples demonstrate consistency across replicates. Each replicate represents pooled data from 5-8 animals/condition. See Methods for details.

D) Feature plots of data in Fig. 2.1B, showing representative genes used for cell-type assignment. *Ptprc* hematopoietic cells; *H2-Aa*: MHC class II^{+} myeloid subsets; *Itgam:* macrophage subsets; *Il7ra:* lymphocytes; *Cd19:* B lymphocytes; *Pdgfra:* stromal cells.

E) Feature plot highlighting *Il33* expression, enriched in meningeal stromal cell subsets.

F) Volcano plot showing differentially expressed genes in ILC2s from IL-33-deficient ($Il33^{mCherry/mCherry}$) vs. IL-33 heterozygote ($Il33^{wt/mCherry}$) mice. Black dots = $\log_e$ fold change (FC) cutoff at 0.2. Select genes highlighted in red.

G) *Il13* and *Il4* transcript expression in lymphocytes from P14 meninges by genotype.

H) Flow cytometry gating strategy for analysis of lymphocyte subsets in Fig. 2.1F-G.

Supplemental Table 2.1: Cluster defining genes for all meningeal cells scRNASeq: Differential gene expression analysis for P14 meninges single cell RNA-seq clustering, related to Fig. 2.1B and 2.2D.

Supplemental Table 2.2: Cluster defining genes for meningeal lymphocyte scRNASeq: Differential gene expression analysis for non-B lymphocytes (cluster 9 in Fig. 1B) from P14 meninges single cell RNA-seq clustering, related to Fig. 2.1C and 2.1D.

Chapter 3: Meningeal ILC2s produce elevated IL-13 in early life

To determine if meningeal lymphocytes might play functional roles during CNS development, we next tracked expression of two types of canonical cytokines across early postnatal life. Both the type 1 cytokine Interferon-gamma (IFNγ) and the type 2 cytokine IL-13 are predominantly produced by non-B lymphocytes and signal to a diverse array of endothelial, stromal, immune, and tissue effector cell types (*e.g.* neurons). We examined type 2 immune activation over development using sensitive transcriptional reporter mice for IL-13 *(Il13^{huCD4})* and IL-5 (*Il5$^{Cre\text{-}RFP}$*; **Fig. 3.1A**). We identified ILC2s with an Arginase-1 reporter (*Arg1^{YFP}),* as meningeal ILC2s express constitutive *Arg1* as in other tissues (Schneider et al., 2019). ILC2s produced a wave of IL-13 and IL-5 activity between postnatal days 5-15 (**Fig. 3.1B-D, 3.2A**). In contrast, adaptive T cells did not express any detectable reporter over this same period (**Fig. 3.2A-B**). Using sensitive IL-5 lineage tracker mice (*Il5$^{Cre\text{-}RFP}$;R26^{tdTomato})*, we confirmed that ST2$^+$ ILC2s accounted for over 80% of meningeal IL-5$^+$ lymphocytes whereas only a small fraction were T cells (~9%; **Fig. 3.2C**).

In contrast to the temporally restricted burst of IL-5 and IL-13, the canonical type 1 cytokine IFNγ (*IFNγ^{YFP}*, **Fig. 3.2D-E**) was constitutively expressed in meningeal NK/ILC1 cells (NK1.1$^+$ CD3e$^-$). This expression was present from early life and gradually increased into adulthood, mirroring the expression of IFNγ in subsets of CD4$^+$ and CD8$^+$ T cells (**Fig. 3.2F-G**).

Next, we used confocal imaging to identify meningeal ILC2s *in situ,* using *Il5$^{Cre\text{-}RFP}$;R26^{tdTomato}* lineage tracker mice. Few IL-5$^+$ cells were present shortly after birth (P1-2). By P14, IL-5$^+$ cells expanded predominantly in smooth muscle actin-α (αSMA)-rich adventitial regions around the dural sinus and other large vasculature (**Fig. 3.1E-F**). These regions are immune hubs where

CNS-associated interstitial fluid reaches draining lymphatics and coordinates neuro-immune signaling (Alves De Lima et al., 2020; Rustenhoven et al., 2021; Dahlgren et al., 2019). Together, these results suggest that early-life tissue immune activation is skewed towards type 2 cells (ILC2s) and cytokine release (IL-5/IL-13). ILC2s expand in meningeal immune hubs and produce a wave of IL-13 in early life, suggesting they could be a relevant source of immune signals during postnatal brain development.

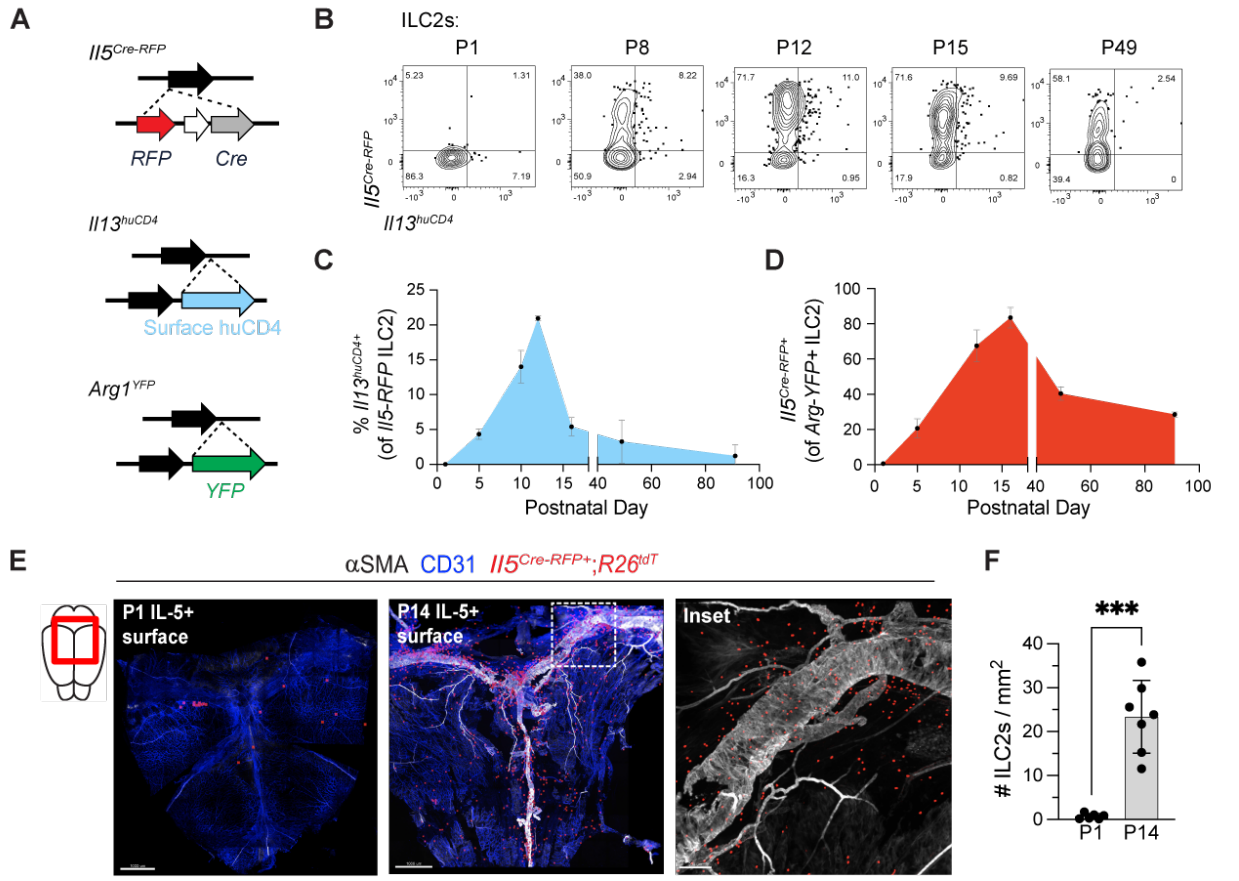

Figure 3.1: Meningeal ILC2s produce elevated IL-13 in early life.

A) Schematics depicting cytokine reporter constructs in relation to their respective endogenous murine loci. Note that *Il5*$^{Cre\text{-}RFP}$ leads to loss of function of the endogenous locus whereas *Il13*^{huCD4} *and Arg1*^{YFP} are inserted into the 3' untranslated region and preserve gene expression. *huCD4*: human CD4.

B) Representative flow plots showing expression of IL-5 (*Il5*$^{Cre\text{-}RFP}$) and IL-13 (*Il13*^{huCD4}) within Arg1^{YFP+} meningeal ILC2s across development. Gating strategy used to identify ILC2s and specificity of Arg1^{YFP} shown in Fig. 3.2A.

C) Quantification of IL-13 expression in meningeal ILC2s over development (percent *Il13*$^{huCD4+}$ of *Arg1*$^{YFP+}$ *Il5*$^{Cre\text{-}RFP+}$ ILC2s; Number of mice per age: P1 n=3; P5 n=2; P10 n=3; P12 n=2; P16 n=3; P49 n=3; P91 n=4).

D) Quantification of meningeal ILC2 IL-5 expression over development (percent *Il5*$^{RFP+}$ *of Arg1*$^{YFP+}$ ILC2s; Number of mice per age: P1 n=3; P5 n=2; P12 n=2; P16 n=3; P49 n=3; P91 n=3).

E) Confocal imaging and surface reconstruction of whole-mount dural meninges, highlighting ILC2s (red, *Il5*$^{Cre\text{-}RFP}$*:R26*^{TdTomato}), vasculature (blue, CD31) and smooth muscle (white, αSMA) at age P1 and P14. Inset of P14 at the transverse sinus showing native *Il5*$^{Cre\text{-}RFP}$*:R26*$^{TdTomato+}$ signal. Scale bar: 1 mm (P1, P14) and 200 μm (inset).

F) Quantification of meningeal ILC2s (*Il5*$^{Cre\text{-}RFP}$*:R26*$^{TdTomato+}$) at P1 and P14, normalized per area of tissue (P1 n=6, P14 n=7; Dots represent mice. Unpaired t test; ***p < 0.001). Data are mean ± SD.

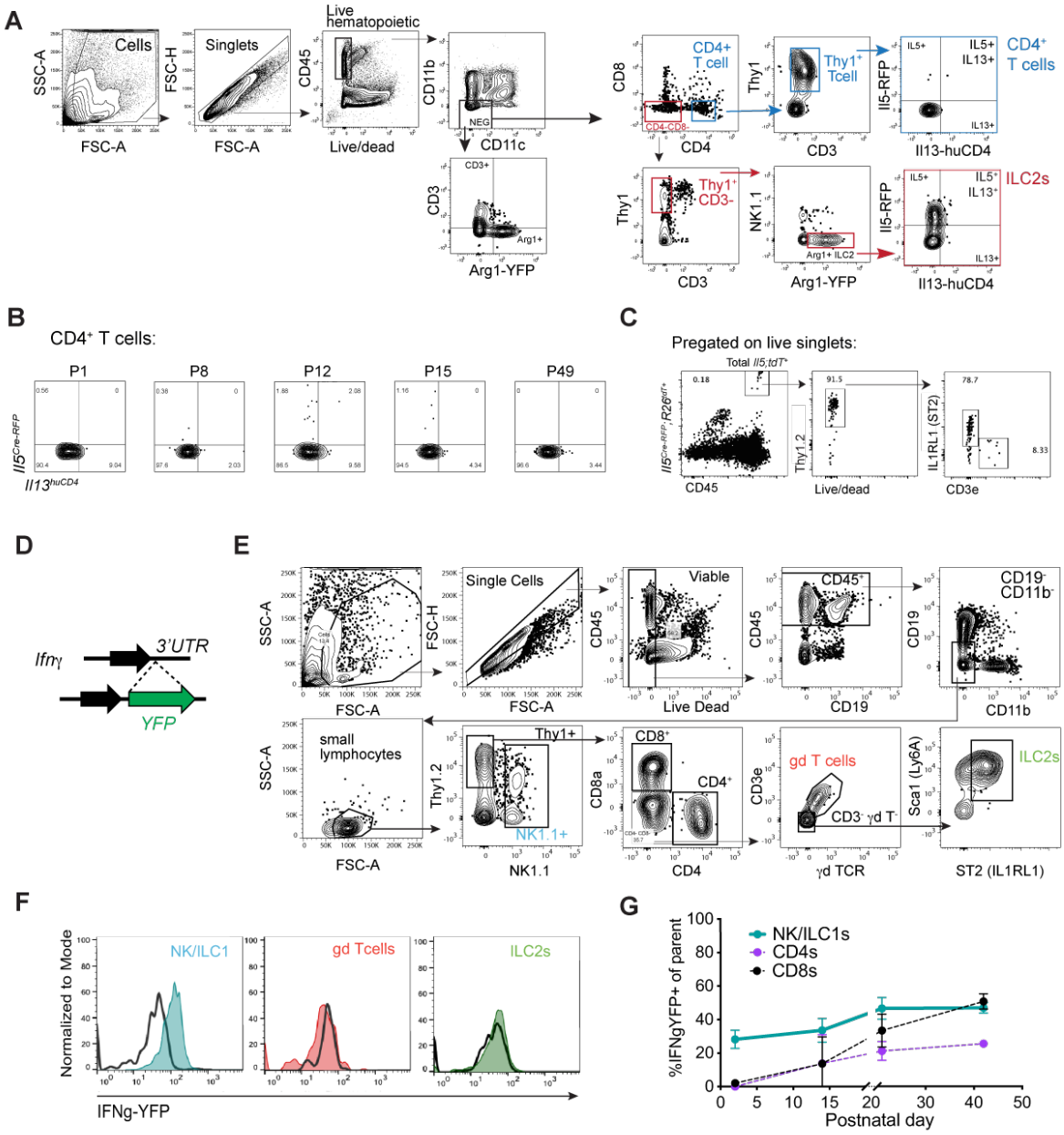

Figure 3.2: Gating strategies and additional cytokine reporter comparisons.

A) Flow cytometric gating strategy for identification of meningeal ILC2s and CD4 T cells in *Arg1*$^{YFP/YFP}$*; Il5*$^{Cre\text{-}RFP/+}$*; Il13*$^{huCD4/+}$ mice. ILC2 gating strategy in red, CD4 T cell gating strategy in blue.

B) Representative flow plots showing expression of IL-5 (*Il5*$^{Cre\text{-}RFP}$) and IL-13 (*Il13*^{huCD4}) in meningeal Thy1^{+} CD4^{+} T cells across development.

C) Representative flow plots from meninges of *Il5*$^{Cre\text{-}RFP}$*:R26*^{TdTomato} lineage tracker mice, demonstrating a majority of *Il5*$^{Cre\text{-}RFP}$*:R26*$^{TdTomato+}$ hematopoietic cells are ILC2s (e.g. Thy1^{+} IL1RL1/ST2^{+}).

D) Schematic depicting *Ifng*^{YFP} genetic construct inserted in the 3'UTR of the murine *Ifng* locus.

E) Gating strategy of meningeal lymphocytes in *Ifng*^{YFP} mice, relevant to Figure S2F-G (NK1.1$^+$ ILC1s/NK cells, CD8$^+$ T cells, CD4$^+$ T cells, CD3e$^+$ TCR$\gamma\delta^+$ $\gamma\delta$ T cells, and lineage$^-$ Thy1$^+$ ST2(IL1RL1)$^+$ Sca-1$^+$ ILC2s).

F) Representative flow histograms depicting IFNγ (*Ifng*^{YFP}) expression in meningeal NK/ILC1s (teal), $\gamma\delta$ T cells (salmon), and ILC2s (green) compared to YFP$^-$ WT mice (black line). Quantification of IFNγ (*Ifng*^{YFP}) expression in meningeal NK/ILC1s, CD8$^+$ T cells, and CD4$^+$ T cells over development, defined as percent of cell type positive for *Ifng*^{YFP}. (n=4 mice/age, except P42 n=3). Data are mean ± SD.

Chapter 4: ILC2s promote inhibitory synapse formation during brain development

Meningeal ILC2s produced elevated IL-13 during a critical period of cortical development (P5-15). Both excitatory and inhibitory synapses are forming and maturing in this period, along with ongoing programmed cell death of inhibitory interneurons (Fishell and Kepecs, 2020; Lim et al., 2018). We therefore sought to examine whether ILC2s impacted cortical circuit development. We used a well-characterized genetic deletion model to constitutively ablate ILC2s via expression of diphtheria toxin under control of the *Il5* promoter (*Il5*$^{Cre\text{-}RFP/Cre\text{-}RFP}$*; R26R*$^{DTA/DTA}$), referred to hereafter as "ΔILC2" (**Fig. 4.1A**). This deletion strategy is specific to ILC2s in development and targets some subsets of tissue-enriched, innate-like CD4^{+} Th2 cells in later life (Molofsky et al., 2013; Nussbaum et al., 2013; Dahlgren et al., 2019; Cautivo et al., 2022). As the *Il5*$^{Cre\text{-}RFP}$ construct replaces the endogenous IL-5 locus, all experiments compared ΔILC2 mice to *Il5*$^{Cre\text{-}RFP/Cre\text{-}RFP}$ littermates ("control"). This strategy led to an ~80% depletion of ILC2s without significantly altering other lymphocyte subsets (**Fig. 4.1B-C**; gating strategy as in **Fig. 2.2H**).

We first assessed whether ΔILC2 mice had altered numbers of excitatory and inhibitory synapses in the cortex, a brain region known to be responsive to meningeal cues during development (Borrell and Marín, 2006; Li et al., 2008; Paredes et al., 2006). Synapses were quantified in somatosensory cortex (S1**,** **Fig. 4.1D**) medial to the barrel field. We observed a significant decrease in inhibitory synapses in ΔILC2 mice at P15 as measured by colocalization of the pre- and post-synaptic markers VGAT and Gephyrin (**Fig. 4.1E-F;** quantification in cortical layer 4 (L4)). This decrease in inhibitory synapses was transient: it was most pronounced at P15, trending down at P30, and no longer present in adult animals, with a trend in the opposite direction (**Fig.**

4.1F-H). In contrast, ΔILC2 mice had no significant differences in excitatory thalamocortical synapses ($VGLUT2^+PSD95^+$) in this region despite a modest downward trend (**Fig. 4.1I-L**). We observed a similar magnitude of reduction in inhibitory synapses across both superficial (L2/3) and deeper (L4) cortical layers, both outside and within the barrel field (**Fig. 4.2A**). These data suggest that cortical inhibitory synapses are broadly reduced in the absence of ILC2s. Further, we found that the inhibitory synapse deficit could be largely rescued by the transfer of activated ILC2s into ΔILC2 mice. ILC2s were stimulated to produce cytokine *in vivo* by IL-33 treatment of donor mice (Cautivo et al., 2022), isolated from the lung, and delivered by intracerebroventricular (i.c.v.) injection into P3 or 4 ΔILC2 neonates. Compared to vehicle-injected littermates, mice that received activated ILC2s showed increased inhibitory synapses at P30 (**Fig. 4.1M**).

To assess inhibitory synaptic function in ΔILC2 mice, we performed whole cell patch clamp recordings from excitatory neurons in L4 barrels to quantify miniature inhibitory post-synaptic currents (mIPSCs; **Fig. 4.1N-O**). Analysis of mIPSCs revealed a reduced frequency of events, consistent with a reduction in synapse numbers, whereas amplitude and kinetics were unchanged (**Fig. 4.1P-Q, Fig. 4.2B;** age P30). These alterations in synapse numbers did not appear to be due to changes in inhibitory neuron survival as there was no change in total $GAD67^+$ or PV^+ interneurons at P15, a time point when developmental apoptosis is largely complete and interneuron numbers have stabilized (Lim et al., 2018); **Fig. 4.2C-D**). Taken together, these data revealed a preferential impact of ILC2s on inhibitory synapse formation during a postnatal developmental window that closely follows their peak of IL-13 production.

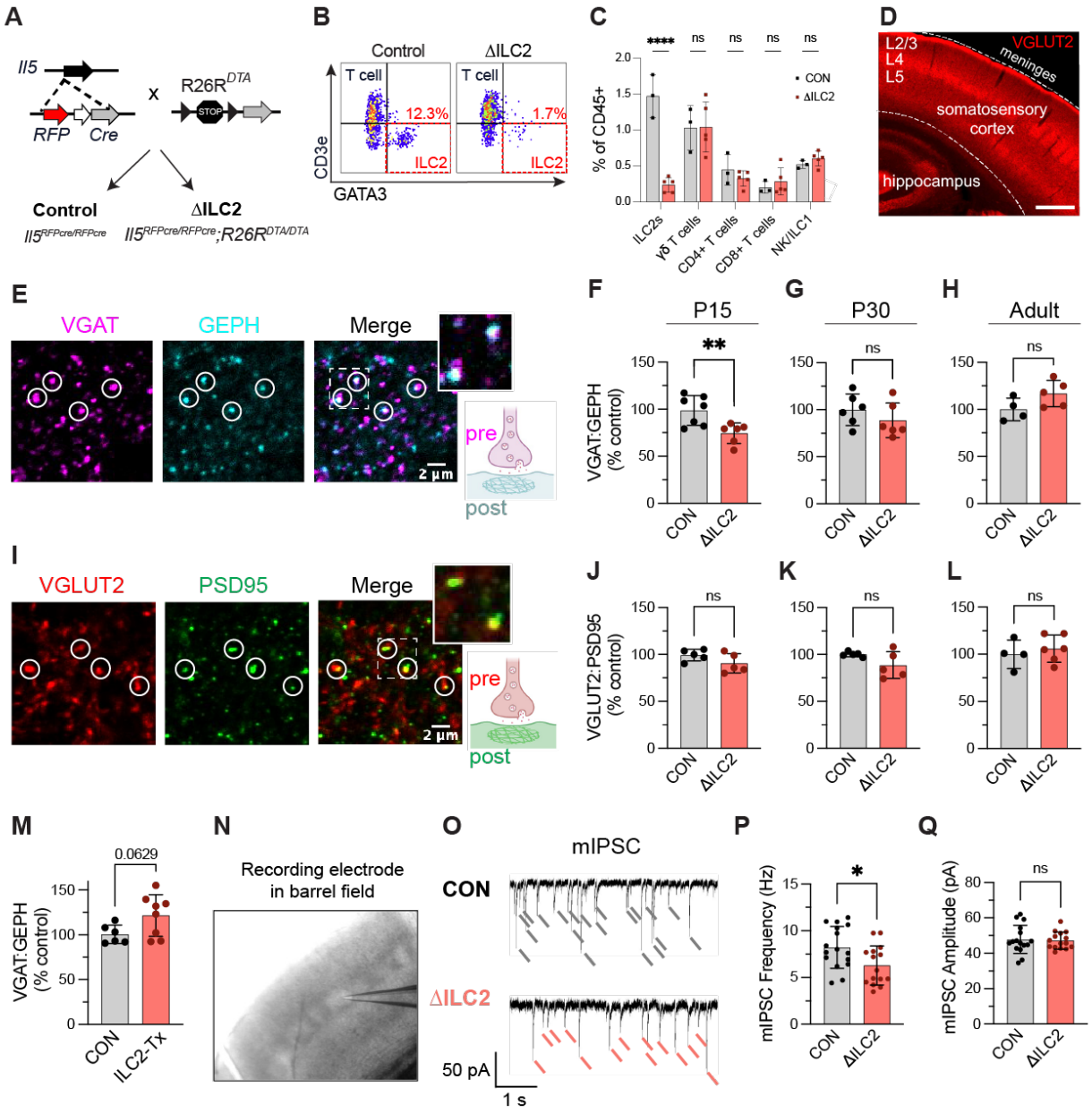

Figure 4.1: ILC2s promote inhibitory synapse formation during brain development.

A) Schematic for generation of ILC2 depleted mice (*Il5*$^{Cre\text{-}RFP/Cre\text{-}RFP}$*:R26R*$^{DTA/DTA}$; a.k.a. "ΔILC2"). All mice were homozygous for *Il5*$^{Cre\text{-}RFP}$; ΔILC2 mice were homozygous for *R26R*^{DTA}, while controls lacked the DTA allele. Littermates used in all experiments unless otherwise noted.

B) Representative flow plots showing depletion of meningeal ILC2s (GATA3^{+}/CD3^{neg}) in ΔILC2 mice compared to controls. Pre-gated on live CD45^{+}CD11b^{-}CD19^{-} cells (see Fig. 2.2H for gating).

C) Quantification of lymphocyte subsets by flow cytometry in ΔILC2 mice as a percentage of controls. Dots represent mice. See gating strategy in Fig. 2.2H. (Age P15; controls n = 3 mice, ΔILC2 n = 5 mice; Two-way ANOVA, Šídák's multiple comparisons test).

D) Representative coronal section depicting primary S1 somatosensory cortex where synaptic quantifications were performed (VGLUT2 used to highlight cortical layers).

E) Representative images of inhibitory synapse immunofluorescence staining of colocalized presynaptic (VGAT) and postsynaptic (Gephyrin, GEPH) markers. Circles indicate examples of colocalized puncta; inset area indicated by white dashed box. (Scale bar: 2 μm; inset: 4x4 μm).

F-H) Quantification of inhibitory synapses (VGAT:GEPH) in layer 4 trunk region S1 cortex at the indicated ages**.** Data at each age is normalized to mean of control group within independent experiments (Adult=12-16 weeks). Dots represent mice. (Mice per age: P15 n = 7 vs. 6; P30 n = 6 vs. 6; Adult n = 4 vs. 5; 2-3 independent experiments; Unpaired t-test).

I) Representative images of thalamocortical excitatory synapses quantified by colocalization of presynaptic (VGLUT2) and postsynaptic ($PSD95^{+}$) markers. Circles indicate examples of colocalized puncta; inset area indicated by white dashed box (Scale bar: 2 μm; inset: 4x4 μm).

J-L) Quantification of excitatory synapses (VGLUT2:PSD95) in layer 4 trunk region S1 cortex at the indicated ages (Adult=12-16 weeks). Dots represent mice. (Mice per age: P15 n = 5 vs. 5; P30 n = 5 vs. 5; Adult n = 4 vs. 6; 2-3 independent experiments; Unpaired t-test).

M) Quantification of inhibitory synapses (VGAT:GEPH) in layer 4 trunk region S1 cortex at P30 after neonatal transfer of ILC2s (ILC2-Tx)**.** Data is normalized to mean of control group within independent experiments. Dots represent mice; n = 6 vs. 8 per group; 2 independent experiments; Unpaired t-test).

N) Image of acute cortical slice used for whole-cell patch-clamp recordings from excitatory neurons in the somatosensory barrel cortex.

O) Representative traces of miniature inhibitory postsynaptic current (mIPSC) recordings from acute brain slices of control and ΔILC2 mice.

P-Q) Quantification of mIPSC frequency (Hz) and amplitude (pA) from the indicated genotypes (Dots represent neurons; n = 16 neurons from 4 controls, and 15 neurons from 4 ΔILC2 mice; Age: P28-30; Unpaired t-test.)

Statistics: *p < 0.05, **p < 0.01, ****p < 0.0001. Data are mean ± SD.

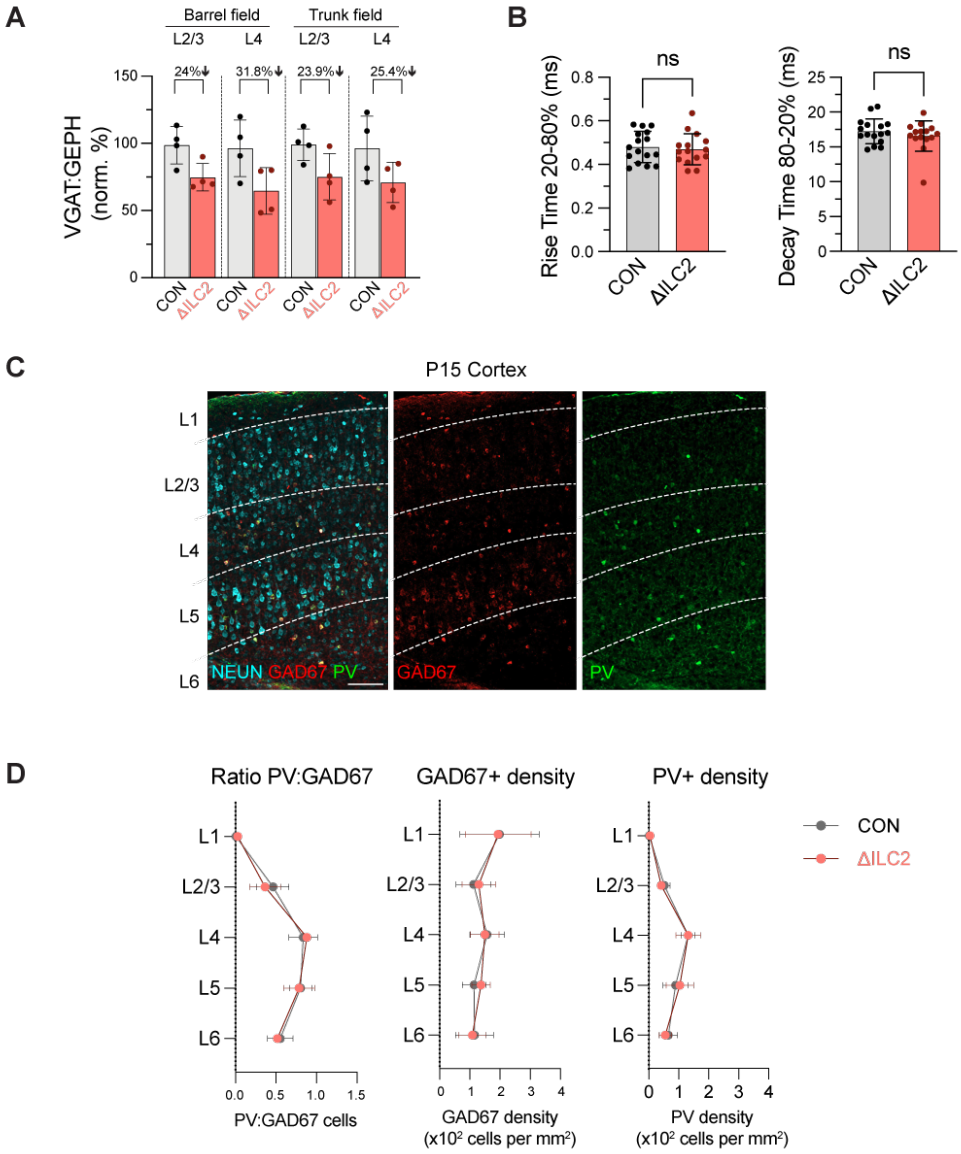

Figure 4.2: Impact of ILC2s on inhibitory synapses and interneuron numbers.

A) Quantification of inhibitory synapses by colocalization of presynaptic (VGAT) and postsynaptic (Gephyrin) markers in multiple S1 layers (L2/3 and L4) and regions. Data normalized to mean of controls within independent experiments. Percent decrease relative to control indicated above each pairwise comparison (Age P15, n=4 mice/genotype, 2 independent experiments. Dots represent mice. Data are mean ± SD)

B) Additional mIPSC parameters from patching experiments in Fig. 4.1P-Q. (Dots represent neurons; n=16 neurons from 4 controls, and 15 neurons from 4 ΔILC2 mice; Age: P28-30; Unpaired t-test. mean ± SD)

C) Representative staining of NEUN (cyan), GAD67 (red), and Parvalbumin (PV, green) in P15 S1 cortex. Scale bar: 100 μm.

D) Quantification of total inhibitory neurons ($GAD67^+$) and Parvalbumin (PV^+) neurons in somatosensory cortex by layer based on immunostaining for the indicated markers. (Age P15; n=5 controls, 4 ΔILC2 mice; 2 independent experiments; Two-way ANOVA, Šídák's multiple comparisons test; Data are mean ± SD.

Chapter 5: ILC2s are required for social recognition memory in adulthood

Transient perturbations in circuit maturation during key developmental windows can result in long-lasting changes in adult behavior (Bitzenhofer et al., 2021; Magno et al., 2021; Reed et al., 2019). Synaptic inhibition in particular plays critical roles in tuning overall network activity. As such, we sought to determine whether the alterations we observed in postnatal development impacted adult behavior. We examined social preference and memory, object recognition, anxiety, and contextual fear memory in ΔILC2 mice and littermate controls (8-14 weeks old). In the three-chamber social interaction test (**Fig. 5.1A**), mice were first habituated to the empty three-chamber field, then allowed to explore the field that contained a novel mouse placed under a wire cup in one chamber and an empty cup in the other. Both ΔILC2 and controls preferred the social cup to the empty cup and spent similar amounts of time interacting with the novel mouse, suggesting intact sociability (**Fig. 5.1B-C**). We also examined social recognition memory 24 hours later by introducing test mice to the same three-chamber apparatus containing the same (familiar) mouse from day 1 in one chamber and a novel mouse in the other (**Fig. 5.1A**). While control mice showed the expected preference for the novel mouse, ΔILC2 mice showed no preference, consistent with impaired social recognition (**Fig. 5.1D-E**).

In contrast to these deficits in social behavior, ΔILC2 mice had intact object memory in the novel object recognition (NOR) assay (**Fig. 5.1F**), with a modest trend towards improved novel object preference compared to controls (**Fig. 5.1G-H**). They also had intact spatial memory and context discrimination, as assessed by a contextual fear conditioning assay, where both groups had similar learning and memory of a foot-shock context (**Fig. 5.2A-B**). We did not observe differences in open field testing or the elevated plus maze assay, indicating normal mobility and anxiety-like

behavior (**Fig. 5.2C-D**). Together, these data reveal that ILC2 deficiency preferentially impacted adult social recognition memory.

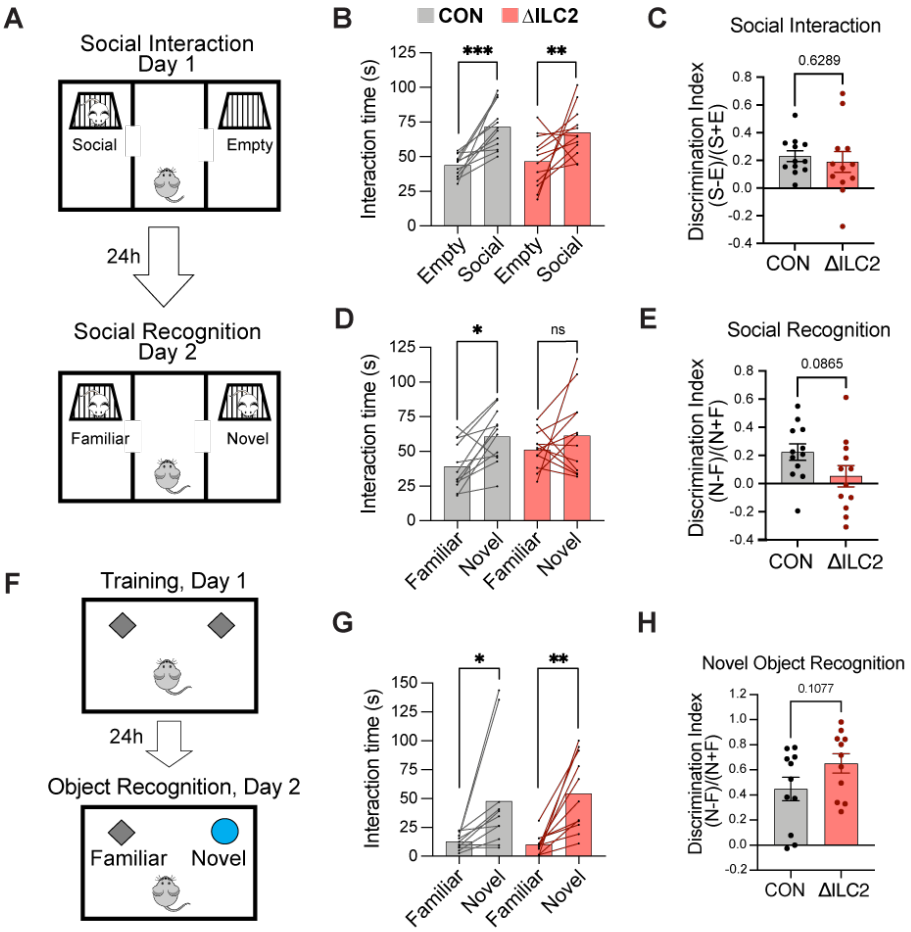

Figure 5.1: ILC2s are required for social recognition memory in adulthood.

A) Schematic of Crawley's three-chamber assay of social interaction (top, Day 1) and social recognition (bottom, Day 2).

B) Interaction time spent with the empty vs. social cup on Day 1 for control mice (*Il5*$^{Cre\text{-}RFP/Cre\text{-}RFP}$) vs. ΔILC2 mice (*Il5*$^{Cre\text{-}RFP/Cre\text{-}RFP}$*:R26R*$^{DTA/DTA}$; Two-way ANOVA, Šídák's multiple comparisons test).

C) The social interaction Discrimination Index calculated as the difference in interaction time with Social (S) and Empty (E) cup, over total interaction time ((S-E)/(S+E); Unpaired t test).

D) Interaction time spent with the familiar vs. novel mouse on Day 2 for control vs. ΔILC2 mice. (Two-way ANOVA, Šídák's multiple comparisons test).

E) The social recognition Discrimination Index calculated as the difference in interaction time with Novel (N) and Familiar (F) cup, over total interaction time ((N-F)/(N+F); Unpaired t test).

F) Schematic of the novel object recognition assay.

G) Interaction time spent with the novel vs. familiar object (Two-way ANOVA, Šídák's multiple comparisons test).

H) The novel object Discrimination Index calculated as the difference in interaction time with novel (N) and Familiar (F) object, over total interaction time ((N-F)/(N+F); Unpaired t test).

Dots represent mice. N=12 mice/genotype for all assays, except novel object recognition (n=11/genotype). Data are means with lines connecting paired data for each mouse (B, D, G) and mean ± SD (C, E, H). *p < 0.05, **p < 0.01, ***p < 0.001.

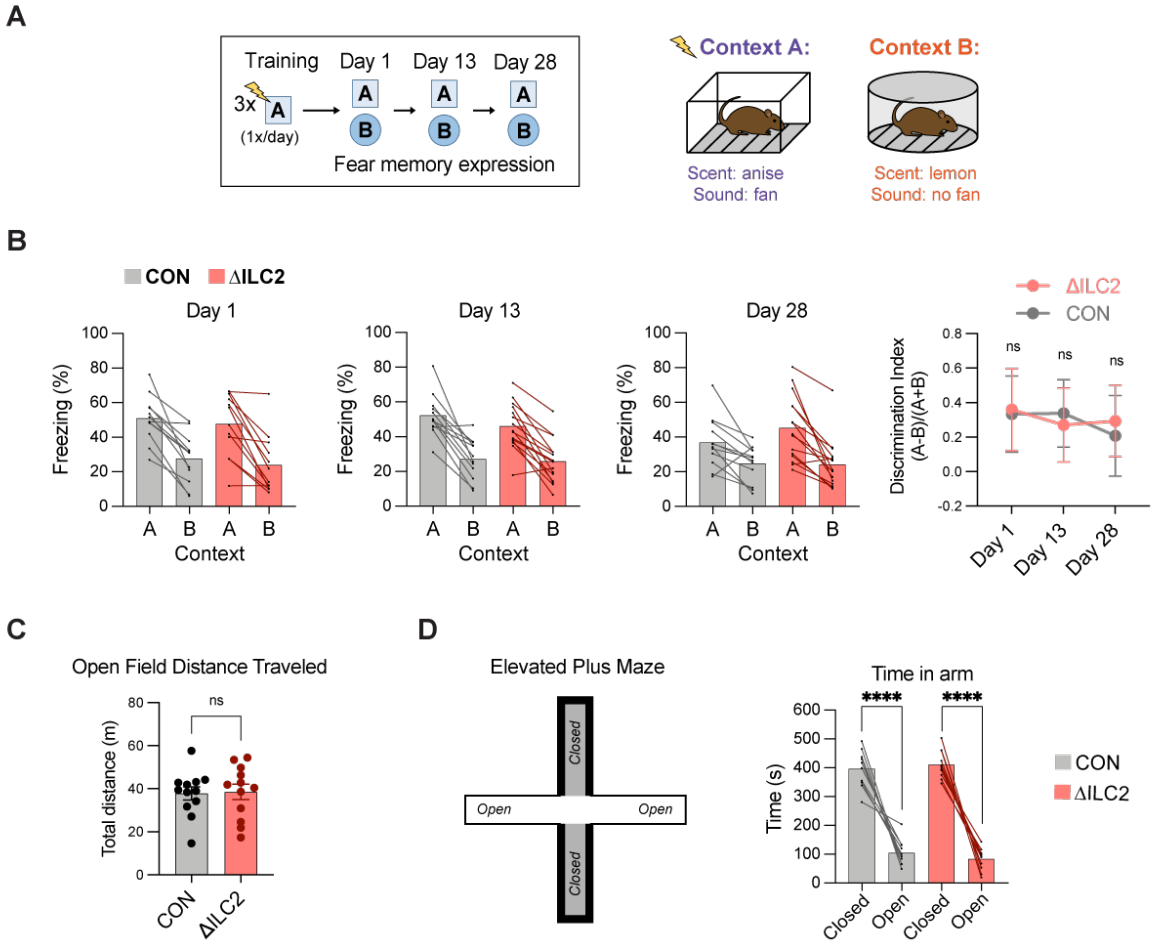

Figure 5.2: Additional behavioral assessments after ILC2 depletion.

A) Schematic of the contextual fear discrimination assay. Mice were conditioned to a context with 1 footshock per day (context A) for 3 days, and then exposed to the conditioned context followed by an unconditioned but partially similar context (context B). Freezing was quantified in each context at 1, 13, and 28 days post-training.

B) Percent of time spent freezing in the conditioned fear context A vs. unconditioned context B during retrieval tests at day 1, 13, and 28 post-training. Far right: the Discrimination Index calculated as the difference in freezing time in Context A and Context B, over total freezing time, ((A-B)/(A+B)) for controls and ΔILC2 mice on retrieval days. (Two-way repeated measures ANOVA, Šídák's multiple comparisons test).

C) Total distance traveled by controls and ΔILC2 mice in the open field assay (Unpaired t test).

D) **Left**: Schematic of the elevated plus maze apparatus. **Right**: Time spent in closed arms vs. open arms by controls and ΔILC2 mice (Two-way ANOVA, Šídák's multiple comparisons test; ****p < 0.0001).

Dots represent mice. N=12 mice/genotype for all assays. Data are means with lines connecting paired data for each mouse (B, D) and mean ± SD (C).

Chapter 6: IL-13/4 signaling to interneurons promotes inhibitory synapse formation and social behavior

Meningeal ILC2s produced a surge of their effector cytokine IL-13 between P5-15, coincident with a reduction in inhibitory synapses at P15 in ILC2-deficient mice. To directly assess whether IL-13 could impact inhibitory synapse numbers, we quantified synapses in both loss- and gain-of-function models. IL-13 signals via a heterodimeric receptor consisting of the IL-13Rα1 and IL-4Rα subunits (**Fig. 6.1A**; (Van Dyken and Locksley, 2013)). Genetic loss of either obligate subunit blocks IL-13 signaling. We found that global deficiency of the *Il4ra* subunit (*Il4ra*$^{-/-}$) phenocopied the reduction of inhibitory synapses seen in ILC2-deficient animals at P15 and did not impact excitatory synapse numbers (**Fig. 6.1B**). Conversely, direct delivery of IL-13 by i.c.v. injection was sufficient to increase inhibitory synapses 20 hours later, and also did not impact excitatory synapse numbers (**Fig. 6.1C**). These data demonstrate that IL-13/4 signaling is sufficient to promote inhibitory synapse formation. While *Il4ra*$^{-/-}$ deletion cannot exclude a role for IL-4, which also signals through IL-4Rα, we did not detect *Il4* transcript in ILC2s or other meningeal lymphocytes (**Fig. 2.2G**). These data suggest that IL-13, which is primarily ILC2-derived, may directly mediate inhibitory synapse formation.

To determine potential targets of IL-13 signaling in the developing cortex, we examined expression of the IL-13 receptor subunit *Il4ra*. *In situ* hybridization revealed *Il4ra* expression throughout somatosensory cortex with enrichment in L4 (Age P30; **Fig. 6.1D**). Almost all microglial and myeloid cells (IBA1^{+}) expressed *Il4ra* (~90%; **Fig. 6.1E,H**), as did subsets of neurons labeled by NEUN (~22%; **Fig. 6.1F,H**) or an interneuron reporter (~23%; *Vgat*$^{Cre/+}$;*R26*$^{tdTomato+}$; **Fig. 6.1G,H**), consistent with published adult datasets (Yao et al., 2021).

Single cell RNAseq of non-neuronal cells in the developing cortex (Dorman et al., 2022) and our meninges scRNAseq dataset confirmed expression of both receptor subunits in myeloid cells, including microglia and meningeal macrophages (**Fig. 6.2A-B**). Therefore, both neurons and myeloid cells are potential cellular targets of IL-13 signaling during development.

To determine whether microglia or macrophages might mediate the impact of IL-13 on inhibitory synapses, and noting their role in inhibitory synaptic remodeling (Favuzzi et al., 2021), we conditionally deleted *Il4ra* in these cell types using a Cre-dependent $Il4ra^{flox}$ strategy (Herbert et al., 2004). While microglia expressed cell surface IL-4Rα and had a robust transcriptional response to exogenous IL-13 *in vivo* **(Fig. 6.2C-D**), we observed some increased variability but no significant changes in inhibitory synapse numbers when we conditionally deleted the IL-13/4 receptor in microglia ($P2ry12^{CreERT}$, **Fig. 6.2E-F**) or in all macrophages ($Cx3cr1^{CreERT}$**, Fig. 6.2G-J**; (Mckinsey et al., 2020; Yona et al., 2013)). Therefore, while myeloid cells could potentially sense IL-13, they were dispensable for its effects on inhibitory synapse formation.

We thus examined whether IL-13 might signal directly to neurons. Given the robust impact of IL-13 on inhibitory synapses, we conditionally deleted *Il4ra* from GABAergic inhibitory neurons using a *Vgat-ires-Cre* allele, a knock-in line that preserves endogenous VGAT function (Vong et al., 2011). These "interneuron *Il4ra* cKO" mice ($Vgat^{Cre/+};Il4ra^{flox/flox}$; **Fig. 6.1I**;) were compared to littermate controls ($Il4ra^{flox/flox}$). We observed significantly fewer inhibitory synapses in interneuron *Il4ra* cKO mice compared to controls at P30, whereas excitatory synapse numbers were not altered (**Fig. 6.1J**). As previously reported, the presence of the *Cre* allele on its own had no effect on synapse numbers (**Fig. 6.2K**). Deletion of *Il4ra* with a pan-neuronal transgenic Cre ($Syn1^{Cre/0};$ $Il4ra^{flox/flox}$; (Zhu et al., 2001)) showed a similar strong trend toward fewer inhibitory synapses

compared to littermate controls (P30, **Fig. 6.2L**). Therefore, IL-13 signaling directly to inhibitory neurons promotes inhibitory synapse formation during development.

Given the similarity in synaptic phenotypes between interneuron *Il4ra* cKO and ΔILC2 mice, we next examined whether loss of IL-13 signaling to interneurons also impacted adult behavior, performing a similar behavioral battery. We found that interneuron *Il4ra* cKO mice had significantly reduced preference for a novel mouse vs. empty cup in the three-chamber social interaction assay (social interaction; **Fig. 6.1K-L**). These mice appeared to have intact social recognition on day two of testing (preference for novel mouse vs. familiar mouse), although interpretation of these results is somewhat complicated by their lack of social preference on day 1 (**Fig. 6.1M-N**). Other behavioral assays did not reveal significant differences (**Fig. 6.2M-N**). Thus, both ILC2 deficiency and loss of IL-13 signaling to interneurons led to a reduction in inhibitory synapses and deficits in social behavior, although there may also be biologically relevant differences in these paradigms that impacted the behavioral readout. Taken as a whole, the data are consistent with a model whereby ILC2-derived IL-13 signals to interneurons to promote inhibitory synapse formation and highlights the impact of these pathways on adult social behavior (**Fig. 7.1)**.

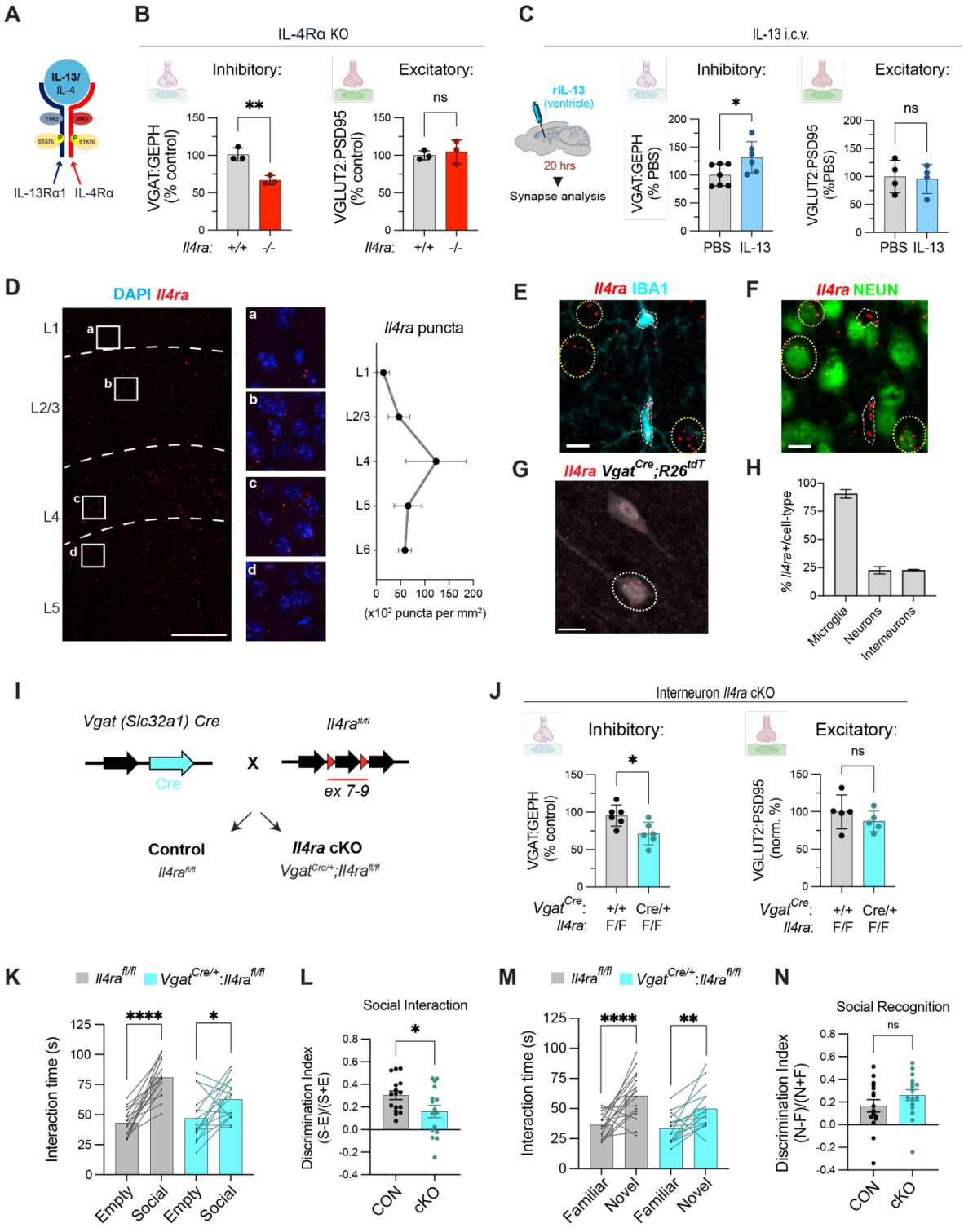

Figure 6.1: IL-13/4 signaling to interneurons promotes inhibitory synapse formation and social behavior.

A) Schematic of the IL-13/4 receptor consisting of the IL-13Rα1 and IL-4Rα subunits.

B) Quantification of inhibitory (VGAT^{+}GEPH^{+}) and excitatory (VGLUT2^{+}PSD95^{+}) synapses in *Il4ra*$^{+/+}$ vs. *Il4ra*$^{-/-}$ mice (Age P15, L4 S1 trunk cortex; n=3 mice per group; Unpaired t test).

C) Quantification of inhibitory and excitatory synapses 20 hours post-i.c.v. injection of IL-13 (250 ng) or PBS (Age P15, L4 S1 trunk cortex; Inhibitory: n=7 control, n=6 IL-13-injected mice; Excitatory: n=4 mice per group; 3 independent experiments; Unpaired t test).

D) Quantitative *in situ* hybridization for *Il4ra* counterstained with DAPI in the somatosensory cortex. Insets (a-d) highlight cortical layers (Age P30; 20X tiled image; scale bar: 100 μm). **Right**: Quantification of *Il4ra* puncta density by layer (n=3 mice; Age P30-60; Dots represent mean.).

E) Representative image showing colocalization of *Il4ra* transcript with microglia (IBA1^{+}; scale bar: 10 μm).

F) Representative image showing colocalization of *Il4ra* transcript with neurons (NEUN^{+};scale bar: 10 μm).

G) Representative image showing colocalization of *Il4ra* transcript with an inhibitory interneuron reporter line (*Vgat*$^{Cre/+}$;*R26*$^{tdTomato+}$; scale bar: 10 μm).

H) Quantification of percentage of *Il4ra*$^{+}$ cells of total cell-type in somatosensory cortex, as in E-G (n=2 mice).

I) Genetic constructs used to conditionally delete *Il4ra* from inhibitory neurons ("interneuron *Il4ra* cKO"). Cre is inserted after the stop codon of the endogenous *Slc32a1 (Vgat)* locus (Vong et al. 2011). The *Il4ra*^{flox} allele allows Cre-mediated excision and conditional deletion of exons 7-9 of *Il4ra* (Herbert et al 2004).

J) Inhibitory (VGAT^{+}GEPH^{+}) and excitatory (VGLUT2^{+}PSD95^{+}) synapse quantifications in interneuron *Il4ra* cKO vs. control mice (Age P30, L4 S1 trunk cortex; Inhibitory, n=6 mice/genotype; Excitatory, n=5 mice/genotype; 2 independent experiments; Unpaired t tests).

K-N) Crawley's three-chamber assay of social interaction and social recognition in control mice vs. interneuron *Il4ra* cKO mice. Age 8-12 weeks; n=16 mice/genotype; Dots represent mice.

K) Interaction time spent with the empty vs. social cup on Day 1 of the social interaction assay by controls vs. interneuron *Il4ra* cKO mice (Two-way ANOVA, Šídák's multiple comparisons test).

L) The Discrimination Index for social interaction calculated as the difference in interaction time with social (S) vs. empty (E) cup, over total interaction time, for control vs. interneuron *Il4ra* cKO mice ((S-E)/(S+E); Unpaired t test).

M) Interaction time spent with the familiar vs. novel mouse on Day 2 of the social recognition assay by control vs. interneuron *Il4ra* cKO mice (Two-way ANOVA, Šídák's multiple comparisons test).

N) The Discrimination Index for social recognition calculated as the difference in interaction time with novel (N) vs. Familiar (F) cup, over total interaction time, for control vs. cKO mice ((N-F)/(N+F); Unpaired t test).

Data are mean ± SD (B, C, D, H, J, L, N) and mean with lines connecting paired data for each mouse (K, M). *p < 0.05, **p < 0.01, ****p < 0.0001.

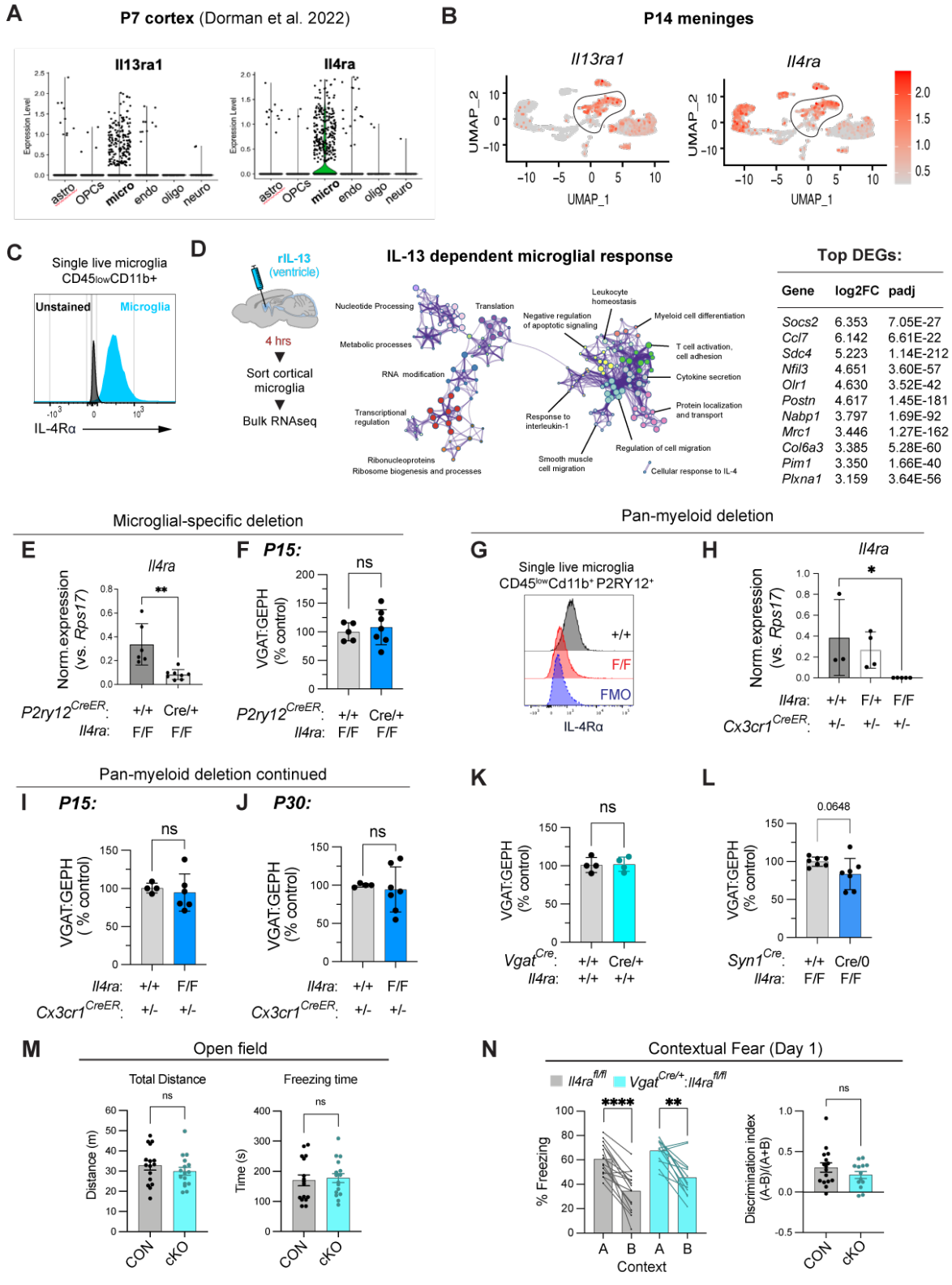

Figure 6.2: Myeloid cells respond to IL-13 but are dispensable for inhibitory synapse formation.

A) Expression of *Il13ra1* and *Il4ra* in single cell RNA sequencing of primarily non-neuronal brain cells at age P7 (generated from (Dorman et al., 2022) dataset).

B) Expression of *Il13ra1* and *Il4ra* in single cell RNA sequencing of meningeal cells at age P14 from data in Fig. 1. Black outline indicates macrophage populations.

C) Representative histogram of flow cytometry data showing protein expression of IL-4Rα in microglia isolated from P15 mice. Microglia (blue, $CD45^{low}$ $CD11b^{+}$) compared to unstained cells (black).

D) Schematic of bulk RNA sequencing experiment after intracerebroventricular injection of IL-13 (250 ng) or PBS in P30 mice (n=4 mice/group). Cortical microglia were FACS sorted 4h post-injection for RNAseq library prep. Center shows Metascape GO term enrichment analysis of differentially upregulated genes (DEGs); Top DEGs shown to right.

E) Quantitative PCR on sorted microglia after conditional deletion of IL-4Rα in microglia (*P2ry12*$^{CreERT/+}$*;Il4ra*$^{flox/flox}$ and *Il4ra*$^{flox/flox}$ mice treated neonatally with tamoxifen; see Methods). *Il4ra* expression normalized to the housekeeper gene *Rps17* (Age P15; n=6 controls, 8 cKOs; 2 independent experiments; Unpaired t test).

F) Inhibitory synapse quantification in microglia-specific *Il4ra* cKO mice (*P2ry12*$^{CreERT/+}$*;Il4ra*$^{flox/flox}$) vs. controls (*Il4ra*$^{flox/flox}$; Age P15; n=5 controls, 7 cKOs; 3 independent experiments; Unpaired t test).

G) Representative flow cytometry histogram of IL-4Rα protein on microglia after conditional *Il4ra* deletion (pre-gated for $CD45^{+}CD11b^{+}P2RY12^{+}$ cells). +/+ control (black, *Cx3cr1*$^{CreERT/+}$*;Il4ra*$^{+/+}$), F/F cKO (red, *Cx3cr1*$^{CreERT/+}$*;Il4ra*$^{flox/flox}$), FMO (blue, fluorescence minus one for IL-4Rα stain on control microglia).

H) Quantitative PCR on sorted microglia after conditional deletion of IL-4Rα in myeloid cells (*Cx3cr1*$^{CreERT/+}$*;Il4ra*$^{flox/flox}$, *Cx3cr1*$^{CreERT/+}$*;Il4ra*$^{flox/+}$, and *Cx3cr1*$^{CreERT/+}$*;Il4ra*$^{+/+}$ mice treated neonatally with tamoxifen; see Methods). *Il4ra* expression normalized to the housekeeper gene *Rps17* (Age P15; n=3 controls, 4 heterozygotes, and 5 cKOS; 3 independent experiments. One-way ANOVA).

I) Inhibitory synapse quantification in pan-myeloid *Il4ra* cKO mice (*Cx3cr1*$^{CreERT/+}$*;Il4ra*$^{flox/flox}$) vs. controls (*Cx3cr1*$^{CreERT/+}$*;Il4ra*$^{+/+}$) at P15 (n=4 controls, 6 cKOs. 3 independent experiments; Unpaired t test).

J) Inhibitory synapse quantification in pan-myeloid *Il4ra* cKO mice (*Cx3cr1*$^{CreERT/+}$*;Il4ra*$^{flox/flox}$) vs. controls (*Cx3cr1*$^{CreERT/+}$*;Il4ra*$^{+/+}$) at P30 (n=4 controls, 7 cKOs. 3 independent experiments; Unpaired t test).

K) Control experiment to assess the impact of *Vgat*^{Cre} allele on inhibitory synapse numbers (comparison of *Vgat*$^{Cre/+}$ vs. wildtype, in the absence of a floxed allele; Age P30; n=4 mice/group; 3 independent experiments; Unpaired t test).

L) Inhibitory synapse quantification in *Syn1*$^{Cre/+}$*:Il4ra*$^{flox/flox}$ pan-neuronal cKO vs. *Il4ra*$^{flox/flox}$ control mice (Age P30; n=7 mice/genotype; 3 independent experiments; Unpaired t test).

M-O) Additional behavioral testing on interneuron *Il4ra* cKO and control mice (Age 8-12 weeks; n=14-16 mice/genotype).

M) Total distance traveled (**left**) and time spent freezing (**right**) in the open field assay by controls and interneuron *Il4ra* cKO mice (n=16 mice/genotype; Unpaired t tests).

N) Mice were conditioned to a context with 1 footshock per day (context A) for 3 days, and then exposed to the conditioned context followed by an unconditioned but partially similar context (context B). **Left**: Freezing was quantified in each context at 1 day post-training (Two-way ANOVA, Šídák's multiple comparisons test). **Right**: The Discrimination Index was calculated as the difference in freezing time in Context A and Context B, over total freezing time on the retrieval day ((A-B)/(A+B); n=14 mice/genotype; Unpaired t test).

Data are mean ± SD and mean with lines connecting paired data for each mouse (N). *p < 0.05, **p < 0.01, ****p < 0.0001.

Chapter 7: Discussion

Despite an emerging recognition of innate lymphocytes as central players in tissue immunity, their essential functions remain somewhat of a mystery, as they seem dispensable in the setting of host defense (Kotas and Locksley, 2018). However, the early abundance of innate lymphocytes relative to adaptive lymphocytes and the finding that they actively produce cytokines in early life have suggested the possibility that they play physiologic roles during development. We observed an expansion of innate lymphocytes in the early postnatal brain meninges, with a marked activation of ILC2s and concurrent IL-13 production, in contrast to adaptive lymphocytes, which were quiescent at this stage and become more abundant than ILCs in adulthood (Mrdjen et al., 2018; Van Hove et al., 2019; Zelco et al., 2021). Similar early-life ILC2 expansion and activation in other tissues suggests a systemic developmental wave (Ricardo-Gonzalez et al., 2018; Schneider et al., 2019). In the lung, a type 2-dominant immune environment in the early postnatal period may have functional implications in antibacterial responses (Saluzzo et al., 2017). It is interesting to speculate that one role of this type 2 developmental wave is to synchronize key developmental events across organ systems.

Within the CNS, we found that the ILC2 developmental wave has a physiologic function – promoting inhibitory synapse formation. Despite the transient impact of ILC2s on inhibitory synapses during development, they were required for social recognition memory in adulthood. Inhibitory interneurons represent a minority (~20%) of cortical neurons, but tuning of inhibitory synapses is a powerful and dynamic way to modulate brain function by synchronizing activity within and between brain regions (Fishell and Kepecs, 2020). These same properties may make them attractive candidates for mediating brain-environment interactions, such as in response to immune challenges and stress (Ansen-Wilson and Lipinski, 2017). Ultimately, and partly

depending on whether these inhibitory changes are operating within or outside of developmental critical periods, alterations in inhibition can have broad impacts, from preventing hyperexcitability and seizures, to more subtle and complex effects on adult social behavior and cognition (Rubenstein, 2010; Sohal and Rubenstein, 2019).

The role of ILC2s in synaptic development and adult social behavior had striking parallels with the phenotypes we observed after eliminating IL-13/4 signaling to inhibitory neurons. Together with other studies that have highlighted a role for IL-13/4 signaling in the brain (Derecki et al., 2010; Herz et al., 2021; Vogelaar et al., 2018; Hanuscheck et al., 2022; Brombacher et al., 2017, 2020; Li et al., 2021), this work reveals an important role for type 2 immune signals in brain function. Although direct signaling to myeloid cells was dispensable for the phenotypes in this study, it is important in other settings, such as injury or neurodegeneration (Taj et al., 2018; Miao et al., 2020; Chen et al., 2022; Kawahara et al., 2012). More broadly, multiple groups have identified cytokine receptor expression on neurons with relevance to brain development and social behavior and direct cytokine signaling to interneurons (Choi et al., 2016; Reed et al., 2019; Filiano et al., 2016; Herz et al., 2021), highlighting the importance of direct neuron-lymphocyte cross-talk in physiologic circuit function.

These findings raise the question of whether type 2 immune signals might impact human social or cognitive development. Brain hyperexcitability is the proximal cause of epileptic seizures, and alterations in excitatory/inhibitory synaptic balance are postulated to underlie diseases including autism spectrum disorder and schizophrenia. While these neurodevelopmental disorders are multifactorial, epidemiologic links to immune dysfunction have repeatedly been observed (Bennett and Molofsky, 2019). Type 2 immunomodulators that could rapidly alter inhibitory tone in the brain might represent a powerful therapeutic strategy in these disorders. These findings also raise the question of how environmental stressors that alter type 2 immune tone (Ruiter et al., 2020) might

impact cognitive or social development. For example, high parasite burden, which is a common feature of childhood in many parts of the world, is frequently associated with delays in learning and cognition (Fernando et al., 2010). Although the psychosocial and metabolic contributions to this effect are complex, directly examining the contributions of immune alterations that might impact brain development could have major impacts on human health.

Limitations of the study: While our study and others demonstrate a role for lymphocyte-derived cytokines in the brain, ILC2s and other lymphocytes are primarily in the dural meninges outside the blood brain barrier (BBB). Emerging evidence suggests that the BBB is dynamic and is permeable to biologically active molecules, though under tight and active control (Yang et al., 2020), thus defining the mechanisms through which these cytokines reach the CNS parenchyma is an essential future direction. Additionally, despite strong concordance in the phenotypes in ILC2-deficient and IL-13/4 deficient mice, there were also some interesting differences in the timing of the synaptic deficits and the features of the social behavioral deficit. This suggests some complexity in the circuit that is not captured in our models, including potential ILC2-independent roles of IL-4 receptor signaling in adulthood (Herz et al., 2021; Hanuscheck et al., 2022). Finally, the impact of IL-13 signaling on inhibitory neuron physiology is of great interest, not only in the setting of neurodevelopment as demonstrated here, but also in settings of injury or disease when reparative cues like IL-13 are induced, such as in traumatic brain injury, stroke, autoimmunity, and neurodegeneration.

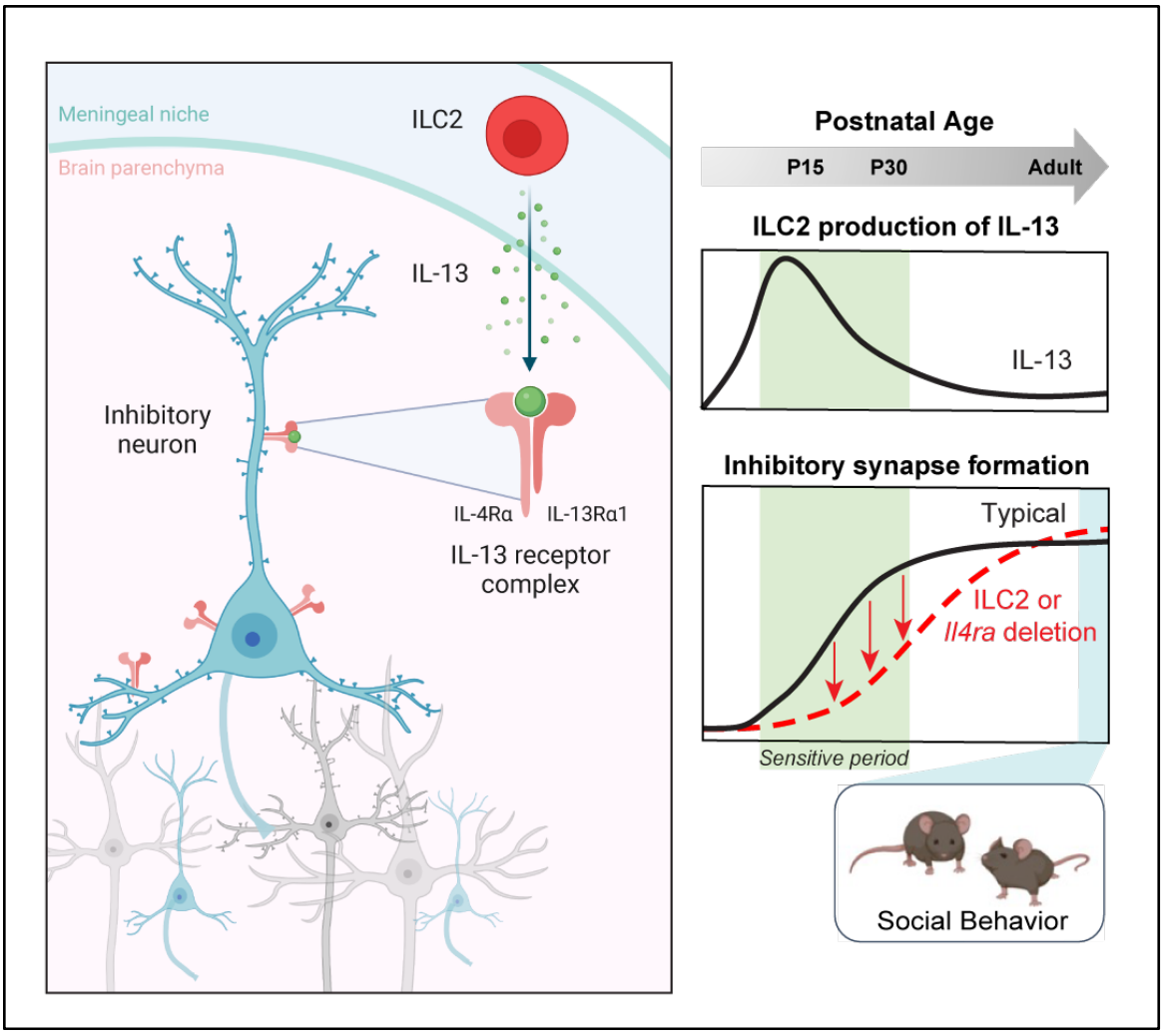

Figure 7.1: Graphical Abstract

A) Group 2 innate lymphoid cells (ILC2s) promote early-life inhibitory synapse development and social behavior**.** This study supports a model in which Interleukin 13 (IL-13) derived from activated, early-life ILC2s signals directly to GABAergic cortical neurons to promote inhibitory synapse maturation. More broadly, they suggest that innate immune signaling can dynamically shape neuronal connectivity during key periods of brain development.

Chapter 8: Materials and Methods

EXPERIMENTAL MODELS AND SUBJECT DETAILS

Mice: All mouse strains were maintained in the University of California, San Francisco specific pathogen–free animal facility, and all animal protocols were approved by and in accordance with the guidelines established by the Institutional Animal Care and Use Committee and Laboratory Animal Resource Center. Littermate controls were used for all experiments when feasible, and all mice were backcrossed > 10 generations on a C57BL/6 background unless otherwise indicated. The mouse strains used are described in the Key Resources Table and as referenced in the text. All experiments, including behavioral analyses, incorporated animals of both sexes in approximately equal numbers. All experiments of n > 5 were analyzed for sex-specific trends, and none were evident unless specifically noted. For experiments using inducible conditional alleles, tamoxifen (Sigma, T5648) was dissolved at 10 mg/ml in corn oil (Sigma-Aldrich, C8267) shaking at 37°C overnight. For conditional deletion of IL-4Rα in myeloid cells (*Cx3cr1*$^{CreER/+}$), mice were intragastrically injected with tamoxifen (50 μg/g body weight) at P1,3,5. For conditional deletion of IL-4Rα in microglia (*P2ry12*^{CreERT}), mice were intragastrically/intraperitoneally injected with tamoxifen (50 μg/g body weight) at P3,5,7 and 100 μg at P11.

METHODS DETAILS

Meningeal dissociation: To prepare single cell suspensions for flow cytometric analysis and sorting, mice were deeply anesthetized and perfused transcardially with cold PBS. Horizontal cuts were made to remove the skullcap which was placed in ice cold FACS Wash Buffer (FWB; 0.1M

DPBS (pH 7.4)/NaN3/3% FBS). Under a dissecting microscope, the dural meninges were quickly removed by gentle scraping using fine forceps and pulled away in an intact sheet. Meninges were kept in ice cold cRPMI (RPMI 1640 supplemented with 10% (vol/vol) FBS, 1% (vol/vol) Hepes, 1% (vol/vol) Sodium Pyruvate, 1% (vol/vol) penicillin-streptomycin) until all samples were isolated. To obtain single cell suspensions, meninges were transferred to cRPMI containing 40ug/mL DNAse I and 0.2 wU/mL Liberase TM in 1 mL of cRPMI and incubated at 37°C with shaking at 220 RPM for 30 min. After gentle trituration, meninges and solution were passed through a 70-μm cell strainer; remaining tissue was firmly pressed through the filter in a circular motion using a wide tip plastic plunger from a 1 ml syringe. The strainer was flushed with additional FWB and collected into a 15 ml falcon tube. Cells were pelleted at 300 RCF for 7 min at 4°C and resuspended in FWB for downstream applications.

Flow cytometry sample preparation: For cell sorting for single cell RNA sequencing, meningeal cell suspensions were incubated with Fc block (2.4G2) and stained with the following antibody solution in FWB (45 min at 4°C): CD45-BUV395, CD31-AF488, CD11b-PB, PDGFRa-APC, gp38-PECy7, DAPI (Antibody details in Key Resources Table). Cells were washed in FWB and fluorescence activated cell sorting was performed on a BD FACS Aria Fusion. Cells were gated for viable single cells and were enriched for lymphocyte and stromal populations by sorting $CD45^{+}CD11b$- (non-myeloid immune cells) and $gp38^{+}CD31$- (stromal cells) separately, and adding each of those populations to 25% of total cells (1:1:2 ratio of lymphocytes: stroma: total viable populations, **Fig. S1A).** Genotypes of mice sequenced were IL-33 deficient (*Il33*$^{mcherry/mcherry}$) or heterozygous controls (*Il33*$^{mcherry/+}$). Meninges from both sexes were pooled by genotype to obtain technical replicates and sufficient numbers of cells for sorting. *Il33*$^{wt/mCherry}$ controls included 5 females and 7 males, and *Il33*$^{mCherry/mCherry}$ knockouts included 7 females and 8 males.

For immunophenotyping over development, flow cytometric analyses were performed. For cytokine reporter tracking, cell suspensions were incubated with a viability dye (Zombie-NIR, 20 minutes), followed by Fc block (2.4G2) and stained with the following antibody solution in FWB (45 min at 4°C): CD45-BUV395, CD3e-AF700, CD4-BV711, CD8a-BV785, Thy1.2-BV421, CD11b-BV605, NK1.1-BV650, CD19-PEDazzle 594, CD11c-PeCy7, CD25-PerCPCy5.5, Hu-CD4-APC (Antibody details in Key Resources Table), followed by wash and resuspension in FWB prior to analysis. Intracellular stains were combined with intravenous labelling of blood circulating cells. Three minutes prior to euthanasia, mice were administered intravenous CD45.2- APCCy7 to label blood circulating cells. Cell suspensions were incubated with a viability dye (Live/Dead Aqua, 20 minutes), followed by Fc block (2.4G2) and surface marker staining with the following antibody solution in FWB (45 min at 4°C): CD45-BUV395, CD3e-AF700, CD4-BV711, CD8a-BV785, Thy1-BV421/PB, CD11b-BV605, TCR γ/δ-PerCPCy5.5, NK1.1-BV650, CD19-PEDazzle 594 (Antibody details in Key Resources Table). Cells were washed in FWB and fixed and permeabilized (60 min at RT) using the FoxP3/transcription factor staining buffer set (eBioscience), followed by intracellular staining with the following antibody solution in 1x PermBuffer (eBioscience) supplemented with 5% rat serum): Rorγt-APC, EOMES-FITC, Tbet-PeCy7, GATA3-PE (60 min at 4°C). Cells were washed two times in 1x PermBuffer and resuspended in FWB prior to analysis. Flow cytometric analysis was performed on a BD Fortessa and data analysis was performed using FlowJo™ software (BD).

Single cell RNA sequencing and analysis: Approximately 35,000 sorted cells of each sample were loaded per well of the Chromium Chip B (10X Genomics) and libraries were generated using the Single Cell 3' reagent kit v3 (10X Genomics) by the UCSF Institute for Human Genetics Core, according to the manufacturer's instructions. Sequencing was performed on the

NovaSeq 6000 Illumina sequencing platform reaching a mean reads per cell of 48,729 (*Il33*$^{mcherry/+}$) and 51,733 (*Il33*$^{mcherry/mcherry}$).

Sequenced samples were processed using the Cell Ranger 3.0.2 pipeline, aligned to the GRCm38 (mm10) mouse reference genome, and further analyzed using R (v 3.6.1) and Seurat (v 3.1.5, Satija et al., 2015). Each data set was individually processed filtering cells within the following thresholds: mitochondrial content <15%, number of genes >500 and <7500 and hemoglobin content <0.1%. Following quality control filtering, 5950 cells and 6594 cells, respectively, were used for analysis and integration. Samples were individually SCTransform normalized (regressed to mitochondrial content and cell cycle score (G1 and S-phase genes: (G1) *Tacc3, Hmgb3, Hmmr, Nde1, Gtse1, Spag5, Kif22, Tpx2, Birc5, Cdc25b, Ube2s, Cdca3, Adgrg6, Ttk, Brd8, Sfpq, Cdc20, Nek2, Cenpf, Gpsm2, Cks2, Top2a, Ccnb1, Cdca8, Troap, Espl1, Ckap2, Nusap1, Kif23, Kif11, Cenpe, Kif2c, Lbr, Ccna2, Mki67, Bub3, Ccnb2, Cdc25c, Ccnf, Hmgb2, Pttg1, Plk1, Bub1, Ube2c, Kpna2, Gm10184, Arhgap11a*; (S) *Mcm2, Mcm6, Ung, Cdc6, E2f1, Ccne1, Pask, Pcna, Dtl, Hspb8, Rfc4, Slbp, Chaf1a, Exo1, Ccne2*) and integrated based on 3000 anchoring features using the SCTransform workflow (https://satijalab.org/seurat/v3.2/integration.html). Following integration, 30 principal components (PCs) were calculated and the first 20 PCs were used for clustering at a resolution of 0.5. The clusters were identified based on expression of canonical markers. Non-B lymphocytes (cluster9) were further subclustered from the integrated dataset resulting in a total of 477 cells (224, and 253 cells from respective sample) and re-clustered using 2000 variable features and 20 PCs at a resolution of 0.3. Cells were identified as ‘‘female’’ or ‘‘male’’ based on their expression of the gene Xist; any cells expressing one or more counts of Xist were labeled female, while all others were labeled male. We then used these assignments to bioinformatically distinguish replicates for a total of two replicates for genotype, as indicated in Fig. S1C. Differential expression for each cluster shown in plots Fig. 1B and 1C were calculated using the FindAllMarkers function in Seurat

on genes expressed in at least 25% of the cells in that cluster. P-values were calculated on upregulated genes using a Poisson test on genes with >0.25 natural log (base e) fold change. The heatmap was created in Seurat using the top 10 markers per cluster based on log fold change. Differential expression analysis comparing ILC2s from *Il33*$^{mcherry/+}$ and *Il33*$^{mcherry/mcherry}$ were performed through the FindMarkers function, applying a Poisson test using the 'SCT' assay and visualized using ggplot2 (3.3.0).

Whole mount meningeal preparation and immunostaining: For whole mount meninges imaging, neonatal (P1 or P14) mice were perfused transcardially with 5-10 mL of ice-cold 1X PBS followed by 5-10 mL of 4% (weight/volume) paraformaldehyde (PFA). Skullcaps containing dural/arachnoid meninges were separated from the brain/pial membrane and post-fixed in 4% PFA overnight at 4°C with shaking (90 rpm). Skullcaps/meninges were washed with 1X PBS and then incubated in Blocking/Permeabilization Buffer (0.3% Triton X-100, 5% fetal bovine serum (FBS), 0.5% bovine serum albumin (BSA), and 0.05% NaN_3 in PBS) for at least one overnight at 4°C (90 rpm). Skullcaps/meninges were then incubated with primary antibodies in Staining Solution (0.15% Triton X-100, 7.5% FBS, 0.75% BSA, and 0.075% NaN_3 in PBS) for three days at 4°C (90 rpm). Skullcaps/meninges were washed three times in PBS-T (0.15% Triton X-100) for 30 min each at 4°C (90 rpm) and incubated with secondary antibodies in Staining Solution overnight at 4°C. Skullcaps/meninges were washed three times in PBS-T for 30 min each and then incubated with directly conjugated antibodies in Staining Solution overnight at 4°C (90 rpm). Skullcaps/meninges were again washed three times in PBS-T for 30 min each and then stained in DAPI (2 ug/mL in PBS) for 30-60 min at 4°C (90 rpm), and rinsed in 1X PBS. Meninges were then dissected out of skullcaps under a dissecting microscope in a PBS bath and whole mounted onto glass slides. Residual PBS was wicked away and replaced with RIMS (Refractive Index Matching Solution: 80% (w/v) Histodenz in 1X PBS, 0.01% NaN_3, 0.1% Tween20). Meninges were covered with a glass coverslip, sealed, and allowed to clear at least one day prior to imaging.

For meningeal imaging, the following antibodies were used: rat anti-CD31 (clone MEC13.3), goat anti-rat AF647, and mouse anti-smooth muscle actin (αSMA)–AF488 direct conjugate (clone 1A4). See Key Resources Table for antibody details and dilutions.

Brain immunostaining: For all immunostaining experiments, mice were perfused transcardially with 10 mL of ice-cold 1X PBS followed by 10 mL of 4% (weight/volume) paraformaldehyde. Brains were post-fixed in 4% PFA at 4°C for 4-5 hours unless otherwise noted, and cryoprotected in 20% sucrose solution for a minimum of 2 days. Brains were flash frozen and sliced in 40 um-thick coronal sections on a HM440E freezing microtome (GMI Instruments). In some cases, brains were embedded in OCT and stored at -80°C until sectioning in 40 um-thick coronal sections on a CryoStar NX70 Cryostat (Thermo Fisher). For RNAscope experiments, brains were fixed in 4% PFA overnight, cryopreserved and embedded, sliced in 14 um-thin sections and slide-mounted.

Free floating 40 um-thick sections were washed three times with PBS prior to antigen retrieval or blocking to remove cryopreservative. For synaptic stains, antigen retrieval was performed in 0.01M sodium citrate pH 6 (95°C for 10 min), cooled at room temperature for 5 min in solution, and washed three times in PBS. Sections were blocked for one hour at room temperature in Staining Solution (0.4% TritonX-100, 5% normal goat serum, 1X PBS), then stained overnight with primary antibody mix in Staining Solution (rocking at 4°C). Sections were washed three times in PBS-T (0.05% Triton X-100 in 1X PBS) and stained with secondary antibody mix in Staining Solution for 1.5 hours (rocking at room temperature). Sections were washed three times in PBS-T, counterstained with Hoechst or Dapi, and mounted onto slides with Fluoromount-G (SouthernBiotech #0100-01).

For optimal synapse staining, the following measures were always taken: Antigen retrieval was performed; Staining Solution was made from high purity 10% Triton X-100 Surfact-Amps detergent (ThermoFisher #28314); Antibody mixes were centrifuged at 15,000 RCF for 3 min in 1.5 ml tubes to remove any aggregates.

The following primary antibodies were used: mouse anti-Gephyrin, rabbit anti-VGAT, rabbit anti-PSD95, guinea pig anti-VGLUT2, chicken anti-NeuN, rabbit anti-IBA1, rabbit anti-GAD67, and mouse anti-Parvalbumin. The following secondary antibodies were used: Goat anti-mouse AF647, Goat anti-rabbit AF555, Goat anti-guinea pig AF647, and Goat anti-chicken AF488. See Key Resources Table for antibody details and dilutions.

RNAscope *in situ* hybridization: FISH experiments were performed using the RNAscope Multiplex Fluorescent Reagent Kit v2 assay (ACD Bio) as described by the manufacturer for fixed-frozen tissue, except tissue was not baked prior to tissue dehydration, antigen retrieval was performed at 80°C, and protease III treatment was reduced to 20 min. Brains were embedded in OCT following 20% sucrose treatment, frozen at -80°C for a minimum of 1 day and then sliced in 14 um-thick coronal sections on a CryoStar NX70 Cryostat (Thermo Fisher) before being mounted on slides for downstream RNAscope processing. Hybridization was performed with the *Mm-Il4ra-C1* probe (ACD Bio, #520171) and TSA Plus Cyanine 3 or Cyanine 5 dye (Perkin Elmer) to detect the receptor subunit transcripts. For immunohistochemical labeling with antibodies following the RNAscope assay, tissues were incubated with blocking and antibody solutions as described above immediately after developing the HRP-TSA Plus signal and washing three times.

Confocal imaging and Image analysis:

Quantification of meningeal ILC2s: Whole mounted meningeal tissues were imaged with a Nikon A1R laser scanning confocal microscope (405, 488, 561, and 650 nm laser lines) using a 16X/0.8 NA Plan Apo water-immersion objective (512 resolution, 1 frame/s, Z step-size = 4um). Z-stack images were rendered into three dimensions and quantitatively analyzed using Bitplane Imaris v9.5.1 software (Andor Technology PLC, Belfast, N. Ireland). 3D reconstructions of ILC2s were generated and quantified using the Imaris surface function on *Il5*-tdTomato^{+} cells, thresholded on signal intensity, volume, and sphericity, as described previously (Dahlgren et al., 2019; Cautivo et al., 2022).

Quantification of synapses: For synaptic puncta quantification, brain sections were imaged on a Zeiss LSM 800 confocal microscope with a 63X/1.4 NA Plan-Apochromat oil-immersion objective. Image acquisition settings: Field size: 101.4 μm x 101.4 μm (10,281.96 μm); Pixel size: ~0.08 μm (1200x1200); Scan speed 4; Averaging: 4; 16 bit; Power, master gain, and digital gain were adjusted for individual experiments and kept consistent within an experiment. Single optical sections were acquired at a consistent depth of 5 μm below the surface to reduce variability of signal. We conducted our analysis in layer 4 of S1 somatosensory cortex medial to the barrel field (**Fig. 3D**) in order to achieve a highly consistent subregion, to avoid anatomical variability (e.g. due to the barrel septa), and due to enrichment of thalamocortical synapses for VGLUT2 analysis. Each image contained only L4 as determined by DAPI nuclei density and NeuN cell bodies if included. For IL-13 i.c.v injection experiments, the same region was quantified at ~100-250 μm from the injection site. Technical replicates consisted of 2 images per brain section, 3 sections per mouse (total 6 images); at least 4 biological replicates per genotype or condition were collected, and littermates were used within independent experiments, unless otherwise noted.

The ImageJ2 plugin PunctaAnalyzer was used to quantify the numbers of synaptic puncta and the colocalization of presynaptic and postsynaptic marker channels, as described previously (Stogsdill et al., 2017; Vainchtein et al., 2018). Pre- and postsynaptic marker pairs for inhibitory (VGAT and Gephyrin) and excitatory thalamocortical (VgluT2 and PSD95) synapses were used. Background subtraction (rolling ball size 50 pixels) was applied, and threshold set to the max tail of the intensity histogram per channel for each image. Puncta counts were normalized to the mean of controls within each experiment.

Quantification of inhibitory neurons: Brain sections were stained for GAD67, Parvalbumin (PV), and NeuN. Sections were imaged on a Zeiss Z2 fluorescent microscope with Apotome using a 20X/0.8 NA Plan-Apochromat air objective. A tiled field was imaged containing S1 somatosensory cortex L1-L6. Images were analyzed in FIJI by manual drawing of ROI containing each cortical layer and counting $GAD67^+$ or PV^+ soma. Density was calculated by dividing number of cells counted over the area of the ROI. All soma were confirmed to be $NeuN^+$. Two images from two brain sections were averaged per animal, from 2 experiments; littermates were used within independent experiments.

Quantification of RNAscope FISH: Hybridized and immunostained slides were imaged on a Zeiss LSM 800 confocal microscope with a 20X/0.8 NA Plan-Apochromat air objective. A tiled Z stack field was imaged containing S1 somatosensory cortex (4-5 μm thick, Z-step size 0.5 μm). Maximum intensity Z projections were created in FIJI. For layer puncta density quantification, an ROI was drawn for each layer and particle analysis was performed to obtain number of puncta per layer ROI. For cell type quantification, total numbers of microglia ($IBA1^+$ soma), neurons ($NeuN^+$ soma), and interneurons (*Vgat*^{Cre};$Ai14^+$ soma) were manually counted within an ROI. Number of microglial and neuronal soma positive for *Il4ra* transcripts (at least 2 puncta localized

to the nucleus) were counted. Density was calculated as counts per area of the ROI analyzed. One tiled image/section, 2 sections/mouse for two mice were counted per condition.

Slice Preparation and Patch-Clamp Electrophysiology: Mice were deeply anesthetized with isoflurane and euthanized. The brain was removed and 250 μm-thick coronal slices were prepared in ice-cold sucrose cutting solution (234 mM sucrose, 2.5 mM KCl, 1.25 mM NaH2PO4, 10 mM MgSO4, 0.5 mM CaCl2, 26 mM NaHCO3, and 10 mM glucose, equilibrated with 95% O2 and 5% CO2, pH 7.4) using a Leica VT1200 microtome (Leica Microsystems). Sections containing Layer IV barrel cortex were incubated for an hour at 32-34ºC and then at room temperature in artificial cerebrospinal fluid (aCSF; 126 mM NaCl, 2.5 mM KCl, 1.25 mM NaH2PO4, 1 mM MgCl2, 2 mM CaCl2, 26 mM NaHCO3, and 10 mM glucose, equilibrated with 95% O2 and 5% CO2, pH 7.4). Recording electrodes were made from borosilicate glass with a resistance 3–5 MU when filled with cesium chloride intracellular solution (129 mM CsCl, 10 mM HEPES, 10 mM EGTA, 5 mM QX-314 Cl, 4 mM MgATP, 2 mM MgCl2, pH adjusted to 7.35 with CsOH; 286 mOsm). Series resistance was monitored in all recordings, and the recordings were excluded from analysis if the series resistance was > 25 MOhm or varied by more than 25%. Recordings were obtained using a MultiClamp 700B microelectrode amplifier (Molecular Devices, Sunnyvale, CA), digitized using Digidata 1550B (Molecular Devices), and acquired at 20 kHz using pClamp 10 software (Molecular Devices). Recordings were performed in voltage-clamp mode at a holding potential of -65 mV and obtained from visually identified spiny stellate cells within the barrels of the barrel cortex. In the presence of aCSF supplemented with 0.5 μM tetrodotoxin (TTX), 20 μM DNQX, and 50 μM APV, miniature inhibitory post-synaptic currents (mIPSCs) were isolated and recorded for 10 minutes. Recordings were analyzed using ClampFit (Molecular Devices) and Wdetecta

software (https://huguenard-lab.stanford.edu/wdetecta.php). Experimenter was blinded to genotype.

Behavioral Assays: Experiments were conducted in 8-12 week old mice by a blinded experimenter. ILC2-deficient and control mice underwent the following assays in order: Open Field Test, Novel Object Recognition, Object Place Recognition, Social Interaction Test, Social Recognition Memory test, Elevated Plus Maze, and Contextual Fear Conditioning. Inhibitory neuronal conditional knockout and control mice underwent the same assays in order except Elevated Plus Maze. To accommodate mice to the experimenter prior to the behavioral testing, mice were handled in their home cage for 8 min per day for 3 days. Testing occurred over 13 days. Mice were habituated to the testing room 1-2h prior to each assay. ANY-maze software (Stoelting Co.) was used in all assays, except where noted, to video record and track mouse movement using automated object detection and zones customized to each apparatus. Tracking plots were checked for accuracy in all assays and retracked when necessary. Manual scoring was performed for some assays to validate accuracy.

Social interaction test : Sociability and preference for social novelty were measured using Crawley's Three-Chamber test in adult (8-12 weeks) mice as described previously (Nadler et al., 2004; Silverman et al., 2010). One day before the test, mice were habituated for 12 min to the three-chamber open field with equally sized and connected chambers. To test sociability, on test day 1, an ovariectomized female mouse (8-12 weeks) was placed in a wire cup in the left or right chamber (Social cup) and an empty wire cup was placed in the opposite chamber (Empty cup). The experimental mice were placed in the center chamber and allowed to freely explore the three-chamber open field for 10 minutes. Their exploration was recorded and tracked using ANY-maze software. The location of the social cup was alternated in the left or right chamber between mice.

The chamber was cleaned thoroughly after each mouse. “Interaction time” was counted when the nose of the test mouse entered the zone drawn immediately around the empty or social cup.

Social recognition memory test: Twenty-four hours after the Social Interaction Test, mice were tested for social memory. The previously presented ovariectomized female from day 1 was placed in the same wire cup (Familiar cup) in the same chamber, and a novel ovariectomized female was placed in the previously empty opposite cup (Novel cup). The experimental mice were placed in the center chamber and allowed to freely explore the three-chamber open field for 10 minutes. Their exploration was recorded and tracked using AnyMaze software.

Open field test: Mice were introduced to an open field chamber and were assessed over a 10 minute exposure. Their exploration was recorded and tracked using AnyMaze software to obtain distance traveled, time spent freezing, and time in the center zone of the field.

Novel object recognition: Novel object recognition was performed as previously described (Antunes and Biala, 2012). The Open Field Test (OFT) served as habituation for novel object recognition test. The day after the OFT, mice were placed in the same open field apparatus that now contained two identical objects and allowed to explore for 7 min. Twenty-four hours later, mice were tested for object memory and presented with one object from the prior day (Familiar) and one new object (Novel). Location of the novel object was alternated between mice. Exploration was recorded and tracked using AnyMaze software. “Interaction time” was counted when the nose of the test mouse entered the zone drawn immediately around the objects. Objects used in the study were small glass jars of different shape and size.

Elevated plus maze: Mice were introduced to an elevated plus maze and were assessed over a 10 minute exposure. Open arms of the maze were identified as the two opposing arms without

walls, and closed arms of the maze were identified as the two opposing arms with walls. Their exploration was recorded and tracked using AnyMaze software to obtain time spent in the open and closed arms of the maze.

Contextual fear conditioning: Conditioned fear was elicited by administering a mild footshock (0.75 mA) following a 3 minute exposure to an array of contextual cues (conditioning chamber, chamber lights, white noise, scent of anise extract) for 3 days. Retrieval of the fear memory was assessed by a 5 minute re-exposure of the animal to the conditioning context in the absence of shock, and freezing (the cessation of all movement outside of respiration) was interpreted as expression of fear memory. Video recordings were acquired and scored automatically in FreezeFrame (Actimetrics). Mice were habituated to transport and holding in a separate room for 1-2 hours prior to all conditioning or retrieval sessions and subjected to three days of handling prior to all behavioral tests. For assessment of fear discrimination, freezing was measured in a context similar to the conditioning context 2 hours later, but with the following variations: the chamber fan was turned off, the scent of lemon extract instead of anise extract was used, and a plastic divider was inserted to make the chamber walls circular and opaque. Freezing in the similar context was tested 2 hours following retrieval testing in the original conditioning context, and animals were rested in a holding room between sessions.

ILC2 transfers: In vivo expansion and activation of ILC2s was performed in *Il5*$^{Cre\text{-}RFP}$;R26$^{TdT/+}$ mice with 3 injections of 500 ng IL-33 as described previously (Cautivo et al., 2022); a booster injection was given 3-4 days prior to transfer. To obtain sufficient cell numbers, lung ILC2s were sorted as viable, lineage negative RFP^{+} cells and collected in complete media. Cells were washed in normal saline and resuspended to 20,000 cells/μl before i.c.v. injection the same day. Saline or 20,000 ILC2s were transferred into ILC2-deficient (ΔILC2) recipient mice at P3-4 (bilateral i.c.v.

injection, 0.5 μl per side). Recipient mice were euthanized at age P30 and brains were taken for histology.

Stereotactic injections: All brain injections were performed with a Kopf stereotaxic apparatus (David Kopf, Tujunga, CA) and a microdispensing pump (World Precision Instruments) holding a Hamilton Syringe (model 701 RN, 10 μl) with a beveled glass needle (~50 mm outer diameter). For intraventricular injections into neonates (P3/4), mice were anesthetized by hypothermia on ice for 3 min. Bilateral i.c.v. injection of cell suspension or saline vehicle (0.5 μl per side) was performed (from lambda: 1.8 mm AP, +/-1 mm ML, -1.55 mm DV). Afterwards, pups were warmed on a heating pad until full recovery before returning to their home cage. For intraventricular injections into juveniles (P14), mice were anesthetized with 1.5% isoflurane at an oxygen flow rate of 1L/min, head-fixed with a stereotaxic frame (for juveniles, size P11), and treated with ophthalmic eye ointment. Fur was shaved and the incision site was sterilized with 70% ethanol and Betadine prior to surgical procedures. Subcutaneous 0.5% lidocaine was administered at the incision site and lack of reflex response was checked. Body temperature was maintained throughout surgery using a heating pad. A hole was drilled in the skull and 1.25 μl of IL-13 (200 ng/μl) or saline was injected (from lambda: 3.7 mm AP, 1 mm ML, -1.75 mm DV) at a rate of 4 nL/sec. The needle was held in place for 5 minutes to allow diffusion and then slowly removed. The incision was closed and mice were allowed to fully recover with heat. Buprenorphine (Henry Schein Animal Health) was administered (0.1 mg/kg) according to approved protocols (briefly, mice were dosed prior to surgery, 4-8h later, and the next morning if needed by intraperitoneal injection).

Bulk RNA sequencing of cortical microglia: Microglia were isolated from cortex, stained with CD45-FITC (1:100, BioLegend) and CD11b-APC (1:100, BioLegend), and sorted on an Aria III

(BD) flow cytometer into RLT plus buffer (QIAGEN), as described previously (Galatro et al., 2017). RNA was isolated from 30000-60000 microglia per sample with the RNeasy® Plus Micro kit (Qiagen). Quality and concentration were determined with the Agilent RNA 6000 Pico kit on a Bioanalyzer (Agilent). All samples had an RNA Integrity Number (RIN) >7. cDNA and libraries were made using the Ovation® RNA-Seq System V2 kit (NuGen) and quality was assessed by Agilent High Sensitivity DNA kit on a Bioanalyzer (Agilent) and quantified by qPCR. Pooled libraries were RNA sequenced on an Illumina HiSeq 4000 paired-end for 125 cycles (PE125) yielding 50-70 million reads per sample.

Bulk RNA sequencing analysis: Quality of reads was evaluated using FastQC (http://www.bioinformatics.babraham.ac.uk/projects/fastqc), all samples passed quality control, and reads were aligned to mm10 (GRCm38; retrieved from Ensembl, version November 2019) using STAR (version 2.5.4b) (Dobin et al., 2013) with '–outFilterMultimapNmax 1' to only keep reads that map one time to the reference genome. Mapped reads were counted using HTSeq (version 0.9.0)(Anders et al., 2015) and DESeq2 package (version 1.24.0) (Love et al., 2014) was used to normalize the raw counts and perform differential gene expression analysis. GO analysis was conducted using the Metascape webpage (https:// www.metascape.org) for genes from the comparison IL-13 versus PBS with adjusted p value < 0.01 and log fold change >1.

QUANTIFICATION AND STATISTICAL ANALYSIS : Graphpad Prism 9.4.1 was used for most statistical analyses. Statistical tests are as described in text and figure legends. RNA-sequencing data was analyzed in R as described in the methods section above.

Data and materials availability: Supplement contains additional data. All data needed to evaluate the conclusions in the paper are present in the paper or the Supplementary Materials. RNA sequencing data is available through GEO #[submission in progress].

Table 8.1: KEY RESOURCES TABLE

REAGENT or RESOURCE	SOURCE	IDENTIFIER
Antibodies		
FLOW CYTOMETRY		
Fc Block	BD Biosciences	Cat# 553141
CD45-BUV395 (1:400)	BD Biosciences	Cat# 564279
CD31-AF488 (1:200)	BioLegend	Cat# 102414
PDGFRa-APC (1:200)	BioLegend	Cat# 135908
gp38-PECy7 (1:200)	BioLegend	Cat# 127412
CD11b-Pacific Blue (1:200)	BioLegend	Cat# 101224
CD11b-BV605 (1:1000)	BD Biosciences	Cat# 563015
CD3e-AF700 (1:200)	BioLegend	Cat# 100216
CD4-BV711 (1:200)	BD Biosciences	Cat# 563050
CD8a-BV785 (1:200)	BioLegend	Cat# 100750
Thy1.2 (CD90.2) - BV421 (1:400)	BioLegend	Cat# 140327
TCR γ/δ-PerCPCy5.5 (1:200)	BioLegend	Cat# 118118
NK1.1-BV 650 (1:400)	BioLegend	Cat# 108736
CD19-PEDazzle 594 (1:400)	BioLegend	Cat# 115554
CD45.2-APC-eFluor780 (1:200)	eBioscience	Cat# 47-0454-82
GATA3-PE (1:100)	eBioscience	Cat# 12-9966-41
Rorγt-APC (1:100)	eBioscience	Cat# 17-6981-82
Tbet-PeCy7 (1:100)	eBioscience	Cat# 25-5825-82
EOMES-AF488 (1:100)	eBioscience	Cat# 53-4875-82
Hu-CD4-APC (1:100)	eBioscience	Cat# 17-0049-42
CD25-PerCPCy5.5 (1:100)	BioLegend	Cat# 102030
CD11c-PeCy7 (1:200)	BioLegend	Cat# 117318
CD124 (IL-4Rα)-biotin	BD Biosciences	Cat# 552508
IMMUNOFLUORESCENCE		
Rat anti-CD31 (clone MEC13.3, 1:200)	BD Biosciences	Cat# 553370
Living Colors anti-DsRed Rabbit Polyclonal Pan Antibody (1:1000)	TaKaRa	Cat# 632496
Mouse anti-smooth muscle actin (αSMA)–AF488 (clone 1A4, 1:200)	eBioscience	Cat# 53-9760-82
Mouse anti-Gephyrin (1:300)	Synaptic Systems	Cat# 131003
Rabbit anti-VGAT (1:2000)	Synaptic Systems	Cat# 147021
Rabbit anti-PSD95 (1:300)	Invitrogen	Cat# 51-6900

Guinea pig anti-VGLUT2 (1:2000)	Synaptic Systems	Cat# 135404
Chicken anti-NeuN (1:1000)	Millipore	Cat# ABN91; RRID:AB_11205760
Rabbit anti-Iba1 (1:1000)	Wako Chemicals	Cat# 019-19741; RRID:AB_839504
Rabbit anti-GAD67 (1:500)	Invitrogen	Cat# PA521397
Mouse anti-Parvalbumin (1:2000)	Sigma Aldrich	Cat# P3088-100UL
Goat anti-rat AF647 (1:400)	Thermo Fisher	Cat# **A-21247**
Goat anti-chicken AF488 (1:500)	Thermo Fisher	Cat# A-11039
Goat anti-guinea pig AF647 (1:500)	Thermo Fisher	Cat# A-21450
Goat anti-rabbit AF555 (1:500)	Thermo Fisher	Cat# A-21428
Goat anti-rabbit AF488 (1:500)	Thermo Fisher	Cat# A-11034
Goat anti-mouse AF647 (1:500)	Thermo Fisher	Cat# A-21236
Chemicals, peptides, and recombinant proteins		
Recombinant IL-13, carrier free	Biolegend	Cat# 575904
DAPI	Sigma	Cat# D9542-10MG
Live/Dead Fixable Aqua stain (1:1000)	Invitrogen	Cat# L34957
Zombie-NIR fixable dye (1:1000)	Biolegend	Cat# 423105
Tamoxifen	Sigma	Cat# T5648
Critical commercial assays		
RNAscope Multiplex Fluorescent Reagent Kit v2 assay	ACD, Inc.	Cat# 323100
Mouse *Il4ra* RNAscope Probe	ACD, Inc.	Cat# 520171
Deposited data		
Single cell sequencing of P14 meninges (Fig. 1)	This paper.	GEO submission in progress
Bulk RNA sequencing of microglia after vehicle or IL-13 injection (Fig. S5)	This paper.	GEO submission in progress
Experimental models: Organisms/strains		
Mouse: *Il33*^{mcherry} (*Il33*$^{H2B\text{-}mcherry}$)	Vainchtein et al., 2018	Courtesy of Mucosal Immunology Study Team (MIST)
Mouse: *Il5*$^{Cre\text{-}RFP}$ (B6(C)-Il5tm1.1(icre)Lky/J)	Nussbaum JC , et al. 2013	JAX: 030926; RRID:IMSR_JAX:030926
Mouse: *R26*^{TdT} (B6.Cg-Gt(ROSA) 26Sortm14(CAG-tdTomato)Hze/J)	Madisen L , et al. 2010	JAX: 007914; RRID:IMSR_JAX:007914
Mouse: *Arg1*^{YFP} (C.129S4(B6)-*Arg1*$^{tm1.1Lky}$/J)	Reese TA , et al. 2007	JAX: 015858; RRID:IMSR_JAX:015858
Mouse: IL13^{huCD4} (B6.129S4©-*Il13*$^{tm2.1Lky}$/J)	Liang HE , et al. 2011	JAX: 031367; RRID:IMSR_JAX:03136

Mouse: *R26R*$^{DTA/DTA}$ (B6;129-*Gt(ROSA)26Sor*$^{tm1(DTA)Mrc}$/J)	Wu S , et al. 2006	JAX: 010527; RRID:IMSR_JAX:010527
Mouse: *Il4ra*$^{-/-}$ (*Il4ra*^{tm1Fbb})	Mohrs et al. 1999	MGI:2657172
Mouse: *Il4ra*^{flox} (*Il4ra*^{tm2Fbb})	Herbert et al 2004	MGI:3689995
Mouse: *Syn1*^{Cre} (B6.Cg-Tg(*Syn1-cre*)671Jxm/J)	Zhu et al., 2001	JAX: 003966; RRID:IMSR_JAX:003966
Mouse: *Vgat*^{Cre} (B6J.129S6(FVB)-*Slc32a1*$^{tm2(cre)Lowl}$/MwarJ)	Vong L , et al. 2011	JAX: 028862; RRID:IMSR_JAX:028862
Mouse: *Cx3cr1*^{CreER} (B6.129P2(C)-*Cx3cr1*$^{tm2.1(cre/ERT2)Jung}$/J)	Yona et al., 2013	JAX: 020940; RRID:IMSR_JAX:020940
Mouse: *P2ry12*^{CreER} (B6(129S6)-*P2ry12*$^{em1(icre/ERT2)Tda}$/J)	McKinsey et al., 2020	JAX: 034727; RRID:IMSR_JAX:034727
Mouse: C57BL/6J	The Jackson Laboratory	JAX: 000664; RRID:IMSR_JAX:000664 Ovariectomy at 7-8 weeks
Mouse: C57BL/6N	Charles River Laboratories	Ovariectomy at 7-8 weeks
Software and algorithms		
Seurat (v3.1.5)	Satija et al., 2015	
STAR (v2.5.4b)	Dobin et al., 2013	
DESeq2 (v1.24.0)	Love et al., 2014	
ANY-maze	Stoelting Co.	
Prism (v9.4.1)	Graphpad	
FlowJo (v9, v10)	TreeStar, USA	https://www.flowjo.com
Bitplane Imaris (v9.5)	Andor Technology PLC, Belfast, N. Ireland	https://imaris.oxinst.com
BioRender.com		
Other		
FoxP3/Transcription factor staining buffer set	eBioscience	Cat# 00-5523-00

References

Alves de Lima, K., Rustenhoven, J., Da Mesquita, S., Wall, M., Salvador, A.F., Smirnov, I., Martelossi Cebinelli, G., Mamuladze, T., Baker, W., Papadopoulos, Z., Lopes, M.B., Cao, W.S., Xie, X.S., Herz, J., Kipnis, J., 2020. Meningeal γδ T cells regulate anxiety-like behavior via IL-17a signaling in neurons. Nature Immunology 21, 1421–1429. https://doi.org/10.1038/s41590-020-0776-4

Alves De Lima, K., Rustenhoven, J., Kipnis, J., 2020. Meningeal Immunity and Its Function in Maintenance of the Central Nervous System in Health and Disease. Annual Review of Immunology.

Ansen-Wilson, L.J., Lipinski, R.J., 2017. Gene-environment interactions in cortical interneuron development and dysfunction: A review of preclinical studies. NeuroToxicology 58, 120–129. https://doi.org/10.1016/j.neuro.2016.12.002

Antunes, M., Biala, G., 2012. The novel object recognition memory: Neurobiology, test procedure, and its modifications. Cognitive Processing 13, 93–110. https://doi.org/10.1007/s10339-011-0430-z

Bennett, F.C., Molofsky, A.V., 2019. The immune system and psychiatric disease: a basic science perspective. Clinical and Experimental Immunology. https://doi.org/10.1111/cei.13334

Bitzenhofer, S.H., Pöpplau, J.A., Chini, M., Marquardt, A., Hanganu-Opatz, I.L., 2021. A transient developmental increase in prefrontal activity alters network maturation and causes cognitive dysfunction in adult mice. Neuron 109, 1350-1364.e6. https://doi.org/10.1016/j.neuron.2021.02.011

Bohlen, C.J., Friedman, B.A., Dejanovic, B., Sheng, M., 2019. Microglia in Brain Development, Homeostasis, and Neurodegeneration. Annu. Rev. Genet. 53, 263–288. https://doi.org/10.1146/annurev-genet-112618-043515

Borrell, V., Marín, O., 2006. Meninges control tangential migration of hem-derived Cajal-Retzius cells via CXCL12/CXCR4 signaling. Nature Neuroscience 9, 1284–1293. https://doi.org/10.1038/nn1764

Brombacher, T.M., Ajonijebu, D.C., Scibiorek, M., Berkiks, I., Moses, B.O., Mpotje, T., Brombacher, F., 2020. IL-4R α deletion disrupts psychomotor performance and reference memory in mice while sparing behavioural phenotype associated with spatial learning. Brain Behavior and Immunity 0–7.

Brombacher, T.M., Nono, J.K., De Gouveia, K.S., Makena, N., Darby, M., Womersley, J., Tamgue, O., Brombacher, F., 2017. IL-13-Mediated Regulation of Learning and Memory. The Journal of Immunology. https://doi.org/10.4049/jimmunol.1601546

Cautivo, K.M., Matatia, P.R., Lizama, C.O., Mroz, N.M., Dahlgren, M.W., Yu, X., Sbierski-Kind, J., Taruselli, M.T., Brooks, J.F., Wade-Vallance, A., Caryotakis, S.E., Chang, A.A., Liang, H.-E., Zikherman, J., Locksley, R.M., Molofsky, A.B., 2022. Interferon gamma constrains type 2 lymphocyte niche boundaries during mixed inflammation. Immunity 55, 254-271.e7. https://doi.org/10.1016/j.immuni.2021.12.014

Chen, D., Li, J., Huang, Y., Wei, P., Miao, W., Yang, Y., Gao, Y., 2022. Interleukin 13 promotes long-term recovery after ischemic stroke by inhibiting the activation of STAT3. J Neuroinflammation 19, 112. https://doi.org/10.1186/s12974-022-02471-5

Choi, G.B., Yim, Y.S., Wong, H., Kim, S., Kim, H., Kim, S.V., Hoeffer, C.A., Littman, D.R., Huh, J.R., 2016. The maternal interleukin-17a pathway in mice promotes autism-like phenotypes in offspring. Science 351, 933–939. https://doi.org/10.1126/science.aad0314

Dahlgren, M.W., Jones, S.W., Cautivo, K.M., Dubinin, A., Ortiz-Carpena, J.F., Farhat, S., Yu, K.S., Lee, K., Wang, C., Molofsky, A.V., Tward, A.D., Krummel, M.F., Peng, T., Molofsky, A.B., 2019. Adventitial Stromal Cells Define Group 2 Innate Lymphoid Cell Tissue Niches. Immunity 50, 707-722.e6. https://doi.org/10.1016/j.immuni.2019.02.002

Derecki, N.C., Cardani, A.N., Yang, C.H., Quinnies, K.M., Crihfield, A., Lynch, K.R., Kipnis, J., 2010. Regulation of learning and memory by meningeal immunity: a key role for IL-4. J Exp Med 207, 1067–1080. https://doi.org/10.1084/jem.20091419

DeSisto, J., O'Rourke, R., Jones, H.E., Pawlikowski, B., Malek, A.D., Bonney, S., Guimiot, F., Jones, K.L., Siegenthaler, J.A., 2020. Single-Cell Transcriptomic Analyses of the Developing Meninges Reveal Meningeal Fibroblast Diversity and Function. Developmental Cell 54, 43-59.e4. https://doi.org/10.1016/j.devcel.2020.06.009

Dorman, L.C., Nguyen, P.T., Escoubas, C.C., Vainchtein, I.D., Xiao, Y., Lidsky, P.V., Nakajo, H., Silva, N.J., Lagares-Linares, C., Wang, E.Y., Taloma, S.E., Cuevas, B., Nakao-Inoue, H., Rivera, B.M., Schwer, B., Condello, C., Andino, R., Nowakowski, T.J., Molofsky, A.V., 2022. A type I interferon response defines a conserved microglial state required for effective neuronal phagocytosis. bioRxiv. https://doi.org/10.1101/2021.04.29.441889

Favuzzi, E., Huang, S., Saldi, G.A., Binan, L., Ibrahim, L.A., Fernández-Otero, M., Cao, Y., Zeine, A., Sefah, A., Zheng, K., Xu, Q., Khlestova, E., Farhi, S.L., Bonneau, R., Datta, S.R., Stevens, B., Fishell, G., 2021. GABA-receptive microglia selectively sculpt developing inhibitory circuits. Cell 184, 4048-4063.e32. https://doi.org/10.1016/j.cell.2021.06.018

Fernando, S.D., Rodrigo, C., Rajapakse, S., 2010. The "hidden" burden of malaria: cognitive impairment following infection. Malar J 9, 366. https://doi.org/10.1186/1475-2875-9-366

Filiano, A.J., Xu, Y., Tustison, N.J., Marsh, R.L., Baker, W., Smirnov, I., Overall, C.C., Sachin, G.P., Turner, S.D., Weng, Z., Peerzade, S.N., Chen, H., Lee, K.S., Scott, M.M., Beenhakker, M.P., Litvak, V., Kipnis, J., 2016. Unexpected role of interferon-γ in regulating neuronal connectivity and social behaviour. Nature Letter 535, 425–429. https://doi.org/10.1038/nature18626

Fishell, G., Kepecs, A., 2020. Interneuron Types as Attractors and Controllers. Annu. Rev. Neurosci. 43, 1–30. https://doi.org/10.1146/annurev-neuro-070918-050421

Fung, I.T.H., Sankar, P., Zhang, Y., Robison, L.S., Zhao, X., Souza, S.S.D., Salinero, A.E., Wang, Y., Qian, J., Kuentzel, M.L., Chittur, S.V., Temple, S., Zuloaga, K.L., Yang, Q., 2020. Activation of group 2 innate lymphoid cells alleviates aging-associated cognitive decline. Journal of experiment medicine 217.

Gadani, S.P., Smirnov, I., Smith, A.T., Overall, C.C., Kipnis, J., 2016. Characterization of meningeal type 2 innate lymphocytes and their response to CNS injury. The Journal of experimental medicine jem.20161982. https://doi.org/10.1084/jem.20161982

Galatro, T.F., Vainchtein, I.D., Brouwer, N., Boddeke, E.W.G.M., Eggen, B.J.L., 2017. Isolation of Microglia and Immune Infiltrates from Mouse and Primate Central Nervous System. Methods in Molecular Biology 1559, 333–342. https://doi.org/10.1007/978-1-4939-6786-5

Gasteiger, G., Fan, X., Dikiy, S., Lee, S.Y., Rudensky, A.Y., 2015. Tissue residency of innate lymphoid cells in lymphoid and nonlymphoid organs. Science 350, 981–985. https://doi.org/10.1126/science.aac9593

Han, R.T., Vainchtein, I.D., Schlachetzki, J.C.M., Cho, F.S., Dorman, L.C., Johung, T., Ahn, E., Barron, J.T., Nakao-Inoue, H., Joshi, A., Molofsky, Ari.B., Glass, C.K., Paz, J.T., Molofsky, A.V., 2021. Interleukin-33 coordinates a microglial phagocytic response and limits corticothalamic excitability and seizure susceptibility. bioRxiv. https://doi.org/10.1101/2021.08.05.455250

Hanuscheck, N., Thalman, C., Domingues, M., Schmaul, S., Muthuraman, M., Hetsch, F., Ecker, M., Endle, H., Oshaghi, M., Martino, G., Kuhlmann, T., Bozek, K., van Beers, T., Bittner, S., von Engelhardt, J., Vogt, J., Vogelaar, C.F., Zipp, F., 2022. Interleukin-4 receptor signaling modulates neuronal network activity. Journal of Experimental Medicine 219, e20211887. https://doi.org/10.1084/jem.20211887

Herbert, D.R., Hölscher, C., Mohrs, M., Arendse, B., Schwegmann, A., Radwanska, M., Leeto, M., Kirsch, R., Hall, P., Mossmann, H., Claussen, B., Förster, I., Brombacher, F., 2004. Alternative macrophage activation is essential for survival during schistosomiasis and downmodulates T helper 1 responses and immunopathology. Immunity 20, 623–635. https://doi.org/10.1016/S1074-7613(04)00107-4

Herz, J., Fu, Z., Kim, K., Dykstra, T., Wall, M., Li, H., Salvador, A.F., Zou, B., Yan, N., Blackburn, S.M., Andrews, P.H., Goldman, D.H., Papadopoulos, Z., Smirnov, I., Xie, X.S., Kipnis, J., 2021. GABAergic neuronal IL-4R mediates T cell effect on memory. Neuron 109, 3609-3618.e9. https://doi.org/10.1016/j.neuron.2021.10.022

Kawahara, K., Suenobu, M., Yoshida, A., Koga, K., Hyodo, A., Ohtsuka, H., Kuniyasu, A., Tamamaki, N., Sugimoto, Y., Nakayama, H., 2012. Intracerebral microinjection of interleukin-4/interleukin-13 reduces β-amyloid accumulation in the ipsilateral side and improves cognitive deficits in young amyloid precursor protein 23 mice. Neuroscience 207, 243–260. https://doi.org/10.1016/j.neuroscience.2012.01.049

Kipnis, J., 2016. Multifaceted interactions between adaptive immunity and the central nervous system. Science Neuroimmunology 353, 766–771.

Knuesel, I., Chicha, L., Britschgi, M., Schobel, S.A., Bodmer, M., Hellings, J.A., Toovey, S., Prinssen, E.P., 2014. Maternal immune activation and abnormal brain development across CNS disorders. Nature Reviews Neurology 10, 643–660. https://doi.org/10.1038/nrneurol.2014.187

Kobayashi, T., Voisin, B., Kim, D.Y., Kennedy, E.A., Jo, J.-H., Shih, H.-Y., Truong, A., Doebel, T., Sakamoto, K., Cui, C.-Y., Schlessinger, D., Moro, K., Nakae, S., Horiuchi, K., Zhu, J., Leonard, W.J., Kong, H.H., Nagao, K., 2019. Homeostatic Control of Sebaceous Glands by Innate Lymphoid Cells Regulates Commensal Bacteria Equilibrium. Cell 176, 982-997.e16. https://doi.org/10.1016/j.cell.2018.12.031

Kotas, M.E., Locksley, R.M., 2018. Why Innate Lymphoid Cells? Immunity 48, 1081–1090. https://doi.org/10.1016/j.immuni.2018.06.002

Li, G., Adesnik, H., Li, J., Long, J., Nicoll, R.A., Rubenstein, J.L.R., Pleasure, S.J., 2008. Regional Distribution of Cortical Interneurons and Development of Inhibitory Tone Are Regulated by Cxcl12/Cxcr4 Signaling. Journal of Neuroscience 28, 1085–1098. https://doi.org/10.1523/jneurosci.4602-07.2008

Li, S., olde Heuvel, F., Rehman, R., Li, Z., Aousji, O., Froehlich, A., Zhang, W., Conquest, A., Woelfle, S., Schoen, M., O'Meara, C., Reinhardt, R.L., Voehringer, D., Kassubek, J., Ludolph, A., Huber-Lang, M., Knöll, B., Morganti-Kossmann, M.C., Boeckers, T., Roselli, F., 2021. Interleukin-13 and its receptor are synaptic proteins involved in plasticity and neuroprotection. bioRxiv. https://doi.org/10.1101/2021.12.01.470746

Lim, L., Mi, D., Llorca, A., Marín, O., 2018. Development and Functional Diversification of Cortical Interneurons. Neuron 100, 294–313. https://doi.org/10.1016/j.neuron.2018.10.009

Magno, L., Asgarian, Z., Pendolino, V., Velona, T., Mackintosh, A., Lee, F., Stryjewska, A., Zimmer, C., Guillemot, F., Farrant, M., Clark, B., Kessaris, N., 2021. Transient developmental imbalance of cortical interneuron subtypes presages long-term changes in behavior. Cell Reports 35. https://doi.org/10.1016/j.celrep.2021.109249

Marín, O., 2016. Developmental timing and critical windows for the treatment of psychiatric disorders. Nature Medicine 22, 1229–1238. https://doi.org/10.1038/nm.4225

Mckinsey, G.L., Lizama, C.O., Arnold, T.D., 2020. A New Genetic Strategy for Targeting Microglia in Development and Disease. eLife. https://doi.org/10.1017/CBO9781107415324.004

Miao, W., Zhao, Y., Huang, Y., Chen, D., 2020. IL-13 Ameliorates Neuroinflammation and Promotes Functional Recovery after Traumatic Brain Injury. https://doi.org/10.4049/jimmunol.1900909

Molofsky, A.B., Nussbaum, J.C., Liang, H.-E., Van Dyken, S.J., Cheng, L.E., Mohapatra, A., Chawla, A., Locksley, R.M., 2013. Innate lymphoid type 2 cells sustain visceral adipose tissue eosinophils and alternatively activated macrophages. The Journal of Experimental Medicine 210, 535–549. https://doi.org/10.1084/jem.20121964

Mrdjen, D., Pavlovic, A., Hartmann, F.J., Schreiner, B., Utz, S.G., Leung, B.P., Lelios, I., Heppner, F.L., Kipnis, J., Merkler, D., Greter, M., Becher, B., 2018. High-Dimensional Single-Cell Mapping of Central Nervous System Immune Cells Reveals Distinct Myeloid Subsets in Health, Aging, and Disease. Immunity 0, 1–16. https://doi.org/10.1016/j.immuni.2018.01.011

Nadler, J.J., Moy, S.S., Dold, G., Trang, D., Simmons, N., Perez, A., Young, N.B., Barbaro, R.P., Piven, J., Magnuson, T.R., Crawley, J.N., 2004. Automated apparatus for quantitation of social approach behaviors in mice. Genes, Brain and Behavior 3, 303–314. https://doi.org/10.1111/j.1601-183X.2004.00071.x

Nussbaum, J.C., Van Dyken, S.J., von Moltke, J., Cheng, L.E., Mohapatra, A., Molofsky, A.B., Thornton, E.E., Krummel, M.F., Chawla, A., Liang, H.-E., Locksley, R.M., 2013. Type 2 innate lymphoid cells control eosinophil homeostasis. Nature 502, 245–248.

Paredes, M.F., Li, G., Berger, O., Baraban, S.C., Pleasure, S.J., 2006. Stromal-Derived Factor-1 (CXCL12) Regulates Laminar Position of Cajal-Retzius Cells in Normal and Dysplastic Brains. Journal of Neuroscience 26, 9404–9412. https://doi.org/10.1523/JNEUROSCI.2575-06.2006

Reed, M.D., Yim, Y.S., Wimmer, R.D., Kim, H., Ryu, C., Welch, G.M., Andina, M., King, H.O., Waisman, A., Halassa, M.M., Huh, J.R., Choi, G.B., 2019. IL-17a promotes sociability in mouse models of neurodevelopmental disorders. Nature. https://doi.org/10.1038/s41586-019-1843-6

Ribeiro, M., Brigas, H.C., Temido-ferreira, M., Pousinha, P.A., Regen, T., Santa, C., Coelho, J.E., Marques-morgado, I., Valente, C.A., Omenetti, S., Stockinger, B., Waisman, A.,

Manadas, B., Lopes, L.V., Silva-santos, B., Ribot, J.C., 2019. Meningeal gd T cell – derived IL-17 controls synaptic plasticity and short-term memory. Science Immunology.

Ricardo-Gonzalez, R.R., Van Dyken, S.J., Schneider, C., Lee, J., Nussbaum, J.C., Liang, H.-E., Vaka, D., Eckalbar, W.L., Molofsky, A.B., Erle, D.J., Locksley, R.M., 2018. Tissue signals imprint ILC2 identity with anticipatory function. Nature Immunology. https://doi.org/10.1038/s41590-018-0201-4

Rua, R., McGavern, D.B., 2018. Advances in Meningeal Immunity. Trends in Molecular Medicine 24, 542–559. https://doi.org/10.1016/j.molmed.2018.04.003

Rubenstein, J.L., 2010. Three hypotheses for developmental defects that may underlie some forms of autism spectrum disorder. Current Opinion in Neurology 23, 118–123. https://doi.org/10.1097/WCO.0b013e328336eb13

Rubenstein, J.L.R., Merzenich, M.M., 2003. Model of autism: increased ratio of excitation/inhibition in key neural systems: **Model of autism**. Genes, Brain and Behavior 2, 255–267. https://doi.org/10.1034/j.1601-183X.2003.00037.x

Ruiter, K. de, Jochems, S.P., Tahapary, D.L., Stam, K.A., König, M., van Unen, V., Laban, S., Höllt, T., Mbow, M., Lelieveldt, B.P.F., Koning, F., Sartono, E., Smit, J.W.A., Supali, T., Yazdanbakhsh, M., 2020. Helminth infections drive heterogeneity in human type 2 and regulatory cells. Sci. Transl. Med. 12, eaaw3703. https://doi.org/10.1126/scitranslmed.aaw3703

Rustenhoven, J., Drieu, A., Mamuladze, T., de Lima, K.A., Dykstra, T., Wall, M., Papadopoulos, Z., Kanamori, M., Salvador, A.F., Baker, W., Lemieux, M., Da Mesquita, S., Cugurra, A., Fitzpatrick, J., Sviben, S., Kossina, R., Bayguinov, P., Townsend, R.R., Zhang, Q., Erdmann-Gilmore, P., Smirnov, I., Lopes, M.B., Herz, J., Kipnis, J., 2021. Functional characterization of the dural sinuses as a neuroimmune interface. Cell 184, 1000-1016.e27. https://doi.org/10.1016/j.cell.2020.12.040

Saluzzo, S., Gorki, A.D., Rana, B.M.J., Martins, R., Scanlon, S., Starkl, P., Lakovits, K., Hladik, A., Korosec, A., Sharif, O., Warszawska, J.M., Jolin, H., Mesteri, I., McKenzie, A.N.J., Knapp, S., 2017. First-Breath-Induced Type 2 Pathways Shape the Lung Immune Environment. Cell Reports 18, 1893–1905. https://doi.org/10.1016/j.celrep.2017.01.071

Schneider, C., Lee, J., Koga, S., Ricardo-Gonzalez, R.R., Nussbaum, J.C., Smith, L.K., Villeda, S.A., Liang, H.E., Locksley, R.M., 2019. Tissue-Resident Group 2 Innate Lymphoid Cells Differentiate by Layered Ontogeny and In Situ Perinatal Priming. Immunity 50, 1425-1438.e5. https://doi.org/10.1016/j.immuni.2019.04.019

Silverman, J.L., Yang, M., Lord, C., Crawley, J.N., 2010. Behavioural phenotyping assays for mouse models of autism. Nature Reviews Neuroscience 11, 490–502. https://doi.org/10.1038/nrn2851

Sohal, V.S., Rubenstein, J.L.R., 2019. Excitation-inhibition balance as a framework for investigating mechanisms in neuropsychiatric disorders. Mol Psychiatry 24, 1248–1257. https://doi.org/10.1038/s41380-019-0426-0

Stogsdill, J.A., Ramirez, J., Liu, D., Kim, Y.H., Baldwin, K.T., Enustun, E., Ejikeme, T., Ji, R.R., Eroglu, C., 2017. Astrocytic neuroligins control astrocyte morphogenesis and synaptogenesis. Nature 551, 192–197. https://doi.org/10.1038/nature24638

Taj, S.H., Le Blon, D., Hoornaert, C., Daans, J., Quarta, A., Praet, J., Van der Linden, A., Ponsaerts, P., Hoehn, M., 2018. Targeted intracerebral delivery of the anti-inflammatory cytokine IL13 promotes alternative activation of both microglia and macrophages after stroke. Journal of Neuroinflammation 15, 1–17. https://doi.org/10.1186/s12974-018-1212-7

Vainchtein, I.D., Chin, G., Cho, F.S., Kelley, K.W., Miller, J.G., Chien, E.C., Liddelow, S.A., Nguyen, P.T., Nakao-inoue, H., Dorman, L.C., Akil, O., Joshita, S., Barres, B.A., Paz, J.T., Molofsky, A.B., Molofsky, A.V., 2018. Astrocyte-derived interleukin-33 promotes

microglial synapse engulfment and neural circuit development. Science 1273, 1269–1273.

Van Dyken, S.J., Locksley, R.M., 2013. Interleukin-4- and Interleukin-13-Mediated Alternatively Activated Macrophages: Roles in Homeostasis and Disease. Annual Review of Immunology 31, 317–343. https://doi.org/10.1146/annurev-immunol-032712-095906

Van Dyken, S.J., Nussbaum, J.C., Lee, J., Molofsky, A.B., Liang, H.-E., Pollack, J.L., Gate, R.E., Haliburton, G.E., Ye, C.J., Marson, A., Erle, D.J., Locksley, R.M., 2016. A tissue checkpoint regulates type 2 immunity. Nat Immunol 17, 1381–1387. https://doi.org/10.1038/ni.3582

Van Hove, H., Martens, L., Vlaminck, K.D., Antunes, A.R., Prijck, S.D., Vandamme, N., Schepper, S.D., Scheyltjens, I., Isterdael, G.V., 2019. A single-cell atlas of non-parenchymal brain macrophages reveals unique transcriptional identities that are shaped by ontogeny and tissue environment . Nature Neuroscience 1–44. https://doi.org/10.1038/s41593-019-0393-4

Vogelaar, C.F., Mandal, S., Lerch, S., Birkner, K., Birkenstock, J., Bühler, U., Schnatz, A., Raine, C.S., Bittner, S., Vogt, J., Kipnis, J., Nitsch, R., Zipp, F., 2018. Fast direct neuronal signaling via the IL-4 receptor as therapeutic target in neuroinflammation. Science Translational Medicine 10, 1–13. https://doi.org/10.1126/scitranslmed.aao2304

Vong, L., Ye, C., Yang, Z., Choi, B., Chua, S., Lowell, B.B., 2011. Leptin Action on GABAergic Neurons Prevents Obesity and Reduces Inhibitory Tone to POMC Neurons. Neuron 71, 142–154. https://doi.org/10.1016/j.neuron.2011.05.028

Yang, A.C., Stevens, M.Y., Chen, M.B., Lee, D.P., Stähli, D., Gate, D., Contrepois, K., Chen, W., Iram, T., Zhang, L., Vest, R.T., Chaney, A., Lehallier, B., Olsson, N., du Bois, H., Hsieh, R., Cropper, H.C., Berdnik, D., Li, L., Wang, E.Y., Traber, G.M., Bertozzi, C.R., Luo, J., Snyder, M.P., Elias, J.E., Quake, S.R., James, M.L., Wyss-Coray, T., 2020.

Physiological blood–brain transport is impaired with age by a shift in transcytosis. Nature 583, 1–6. https://doi.org/10.1038/s41586-020-2453-z

Yao, Z., van Velthoven, C.T.J., Nguyen, T.N., Goldy, J., Sedeno-Cortes, A.E., Baftizadeh, F., Bertagnolli, D., Casper, T., Chiang, M., Crichton, K., Ding, S.-L., Fong, O., Garren, E., Glandon, A., Gouwens, N.W., Gray, J., Graybuck, L.T., Hawrylycz, M.J., Hirschstein, D., Kroll, M., Lathia, K., Lee, C., Levi, B., McMillen, D., Mok, S., Pham, T., Ren, Q., Rimorin, C., Shapovalova, N., Sulc, J., Sunkin, S.M., Tieu, M., Torkelson, A., Tung, H., Ward, K., Dee, N., Smith, K.A., Tasic, B., Zeng, H., 2021. A taxonomy of transcriptomic cell types across the isocortex and hippocampal formation. Cell 184, 3222-3241.e26. https://doi.org/10.1016/j.cell.2021.04.021

Yona, S., Kim, K.-W., Wolf, Y., Mildner, A., Varol, D., Breker, M., Strauss-Ayali, D., Viukov, S., Guilliams, M., Misharin, A., Hume, D.A., Perlman, H., Malissen, B., Zelzer, E., Jung, S., 2013. Fate mapping reveals origins and dynamics of monocytes and tissue macrophages under homeostasis. Immunity 38, 79–91. https://doi.org/10.1016/j.immuni.2012.12.001

Zelco, A., Börjesson, V., De Kanter, J.K., Lebrero-Fernandez, C., Lauschke, V.M., Rocha-Ferreira, E., Nilsson, G., Nair, S., Svedin, P., Bemark, M., Hagberg, H., Mallard, C., Holstege, F.C.P., Wang, X., 2021. Single-cell atlas reveals meningeal leukocyte heterogeneity in the developing mouse brain. Genes and Development 35, 1190–1207. https://doi.org/10.1101/gad.348190.120

Zhu, Y., Romero, M.I., Ghosh, P., Ye, Z., Charnay, P., Rushing, E.J., Marth, J.D., Parada, L.F., 2001. Ablation of NF1 function in neurons induces abnormal development of cerebral cortex and reactive gliosis in the brain. Genes Dev. 15, 859–876. https://doi.org/10.1101/gad.862101

Publishing Agreement

It is the policy of the University to encourage open access and broad distribution of all theses, dissertations, and manuscripts. The Graduate Division will facilitate the distribution of UCSF theses, dissertations, and manuscripts to the UCSF Library for open access and distribution. UCSF will make such theses, dissertations, and manuscripts accessible to the public and will take reasonable steps to preserve these works in perpetuity.

I hereby grant the non-exclusive, perpetual right to The Regents of the University of California to reproduce, publicly display, distribute, preserve, and publish copies of my thesis, dissertation, or manuscript in any form or media, now existing or later derived, including access online for teaching, research, and public service purposes.

DocuSigned by:
Jerika Barron
6C4FEF1F7D544E7...
Author Signature

11/29/2022
Date